CrossMark

J. Fluid Mech. (2017), *vol.* 822, *pp.* 139–169. © Cambridge University Press 2017
doi:10.1017/jfm.2017.263

Resonant three-dimensional nonlinear sloshing in a square-base basin. Part 4. Oblique forcing and linear viscous damping

Odd M. Faltinsen[1,†] **and Alexander N. Timokha**[1,2]

[1]Centre for Autonomous Marine Operations and Systems and Department of Marine Technology, Norwegian University of Science and Technology, NO-7491 Trondheim, Norway

[2]Institute of Mathematics, National Academy of Sciences of Ukraine, 01601 Kiev, Ukraine

(Received 14 December 2016; revised 19 April 2017; accepted 19 April 2017; first published online 2 June 2017)

Faltinsen *et al.* (*J. Fluid Mech.*, vol. 487, 2003, pp. 1–42) (henceforth, Part 1) examined an undamped nonlinear resonant steady-state sloshing in a square-base tank by developing an approximate (asymptotic) Narimanov–Moiseev-type multimodal theory. The focus was on longitudinal and diagonal harmonic tank excitations. Neglecting the linear viscous boundary-layer damping was justified for model tanks with breadths of the order of metres. However, nonlinear sloshing in clean tanks of smaller size (count in centimetres) may be affected by damping in finite depth conditions. Qualitative and quantitative properties of the damped resonant steady-state sloshing in a square-base tank are now studied by using the modal theory from Part 1 equipped with the linear damping terms. The tank harmonically oscillates along an arbitrary horizontal (oblique) direction. An analytical asymptotic steady-state undamped solution is derived and the corresponding response curves are analysed versus the forcing direction. When the tank width $=$ breadth $= L \sim 10$ cm, the surface tension effect on the free-surface dynamics can be neglected but the linear viscous damping should be included into the Narimanov–Moiseev nonlinear asymptotic modal theory. We analytically show that the steady-state damped sloshing possesses a series of distinguishing features so that, e.g. the square-like standing wave regime fully disappears and becomes replaced by swirling. Typical response curves of the damped steady-state resonant sloshing are studied for the liquid depth-to-width ratio exceeding 0.5. The computational results of the steady-state resonant response amplitudes are in a satisfactory agreement with observations and measurements by Ikeda *et al.* (*J. Fluid Mech.*, vol. 700, 2012, pp. 304–328), which were conducted with a relatively small laboratory container.

Key words: interfacial flows (free surface)

1. Introduction

Part 1 (Faltinsen, Rognebakke & Timokha 2003) initiated theoretical and experimental studies on the nonlinear resonant liquid sloshing in a square-base tank performing

† Email address for correspondence: odd.faltinsen@ntnu.no

https://doi.org/10.1017/jfm.2017.263 Published online by Cambridge University Press

either longitudinal (along a pair of parallel vertical walls) or diagonal harmonic excitation with the forcing frequency close to the lowest natural sloshing frequency. The theoretical assumptions were (*a*) an ideal incompressible liquid with irrotational flows, i.e. the damping can be neglected; (*b*) the mean liquid depth to the tank breadth L (= width) ratio is finite; (*c*) the surface tension effect on the free-surface dynamics can be neglected; and (*d*) the forcing amplitude is small relative to the tank breadth. The latter non-dimensional forcing amplitude η was associated with a small input parameter $\eta \ll 1$. The assumptions are relevant for many clean (without internal structures, e.g. baffles, screens or bulkheads) rectangular industrial tanks.

By adopting the Narimanov–Moiseev (Duffing-type) asymptotic technique, Part 1 derived a nonlinear approximate (asymptotic) multimodal system governing the generalised coordinates of the nine natural sloshing modes, which are characterised by $O(\eta^{1/3})$, $O(\eta^{2/3})$ and $O(\eta)$. An asymptotic steady-state (periodic) solution of the multimodal system was derived to quantify the frequency ranges where the stable and unstable steady-state resonance wave regimes occur. This steady-state analysis (called the classification) was supported by model tests (Faltinsen *et al.* 2003; Faltinsen, Rognebakke & Timokha 2005*a*) conducted in a rigid tank with a cross-section of 1×1 m. Faltinsen, Rognebakke & Timokha (2005*b*) (Part 2) showed that increasing the forcing amplitude (the input parameter η) requires an adaptive (not Narimanov–Moiseev's one) asymptotic ordering. Using the corresponding adaptive modal systems is also needed for smaller liquid depths and to better describe transient waves. The adaptive ordering accounts for the secondary resonances in the hydrodynamic system. Faltinsen, Rognebakke & Timokha (2006*a*) (Part 3) investigated the aspect ratio effect of the square base.

These studies on resonant sloshing in a square-base tank were followed up by many authors who conducted numerical simulations (Wu & Chen 2009; Wu, Chen & Hung 2013*a*; Wu, Faltinsen & Chen 2013*b*), made new model tests (Ikeda *et al.* 2012) and/or derived their own versions of the (adaptive) multimodal theory (Ikeda *et al.* 2012; Pilipchuk 2013; Zhang, Wu & Liu 2014; Ikeda, Harata & Osasa 2016). In major cases, assumptions (*a*)–(*d*) were common and, therefore, the results were in agreement with Parts 1–3. In particular, they confirmed the established stability ranges for (i) the standing resonant wave occurring in the excitation plane (planar and diagonal for longitudinal and diagonal forcing, respectively), (ii) the square-like sloshing (the standing waves by a combined Stokes mode occurring at an angle to the excitation plane), (iii) the two physically identical (angularly propagating clockwise and counterclockwise) swirling waves, whose wave elevations at the perpendicular walls were equal for the diagonal forcing and (iv) the irregular (chaotic) waves in the frequency ranges where (i)–(iii) are unstable. Against this background, experimental observations and measurements of the steady-state resonant sloshing in a horizontally shaken square-base tank by Ikeda *et al.* (2012) look rather contradictory.

Ikeda *et al.* (2012) investigated the resonant steady-state sloshing for an arbitrary (including oblique) harmonic horizontal forcing and reported that (i′) the purely standing resonant waves in the excitation plane exist exclusively for the longitudinal and diagonal excitations (never for an oblique one), (ii′) the purely square-like standing waves (see, definition in (ii)) do not exist anymore, they are replaced by swirling or, alternatively, by an almost standing wave, which is formally swirling where one of two modified Stokes modes dominates, (iii′) except for the longitudinal forcing, the two physically identical swirling modes of different propagating directions split into two different swirling wave regimes so that, e.g. the maximum wave elevations at the two perpendicular walls become non-equal for the diagonal forcing.

https://doi.org/10.1017/jfm.2017.263 Published online by Cambridge University Press

The differences between (i)–(iii) and (i′)–(iii′) are of a qualitative character and, therefore, they cannot be clarified within the framework of assumptions (*a*)–(*d*). Because (*b*) and (*d*) remain true in these model tests, (*a*) or/and (*c*) must be relaxed to explain the differences.

When the Bond number $Bo = g\rho L^2/T_s$ (g is the gravity acceleration, ρ is the liquid density, T_s is the surface tension) is larger than $\sim 10^3$, the surface tension should not affect, globally, the liquid sloshing dynamics (see, p. 125 in Faltinsen & Timokha 2009). The capillarity can only influence a local flow at the capillary meniscus due to, e.g. the dynamic contact angle effect, which is, according to Shukhmurzaev (1997), a nonlinear phenomenon. When $10^4 \lesssim Bo = g\rho L^2/T_s$, the surface tension effect can be fully neglected in the sloshing problems without a gas mixture. Even though Ikeda *et al.* (2012) used a relatively small laboratory tank with a 0.1×0.1 m square base, computing the Bond number shows that it satisfies the first condition, $10^3 \lesssim Bo$ for the tap water at 20 °C with $T_s = 0.073$ N m^{-1}, $\rho = 10^3$ kg m^{-3} and $g = 9.81$ m s^{-2}. As a consequence, assumption (*c*) is relevant for this experimental case.

Neglecting the linear viscous damping (assumption (*a*)) is rather disputable for small-size tanks. According to Keulegan (1959), the linear laminar viscous boundary-layer damping ratio for a given natural sloshing mode in a rectangular tank with fixed width-to-breadth ratio and liquid depth-to-tank breadth ratio decreases with increasing the breadth L as $1/L^{3/4}$ (see also a discussion in pp. 264–265 by Faltinsen & Timokha 2009). Keulegan (1959) showed experimentally an extra non-negligible contribution due to the dynamic contact angle effect. Hence, when $10^3 \lesssim Bo \lesssim 10^4$, the surface tension quantities can be omitted in the dynamic boundary condition but the related damping may matter. Whether the linear viscous damping indeed matters and clarifies the experimental data by Ikeda *et al.* (2012) is a particular problem, which will be examined in the present paper by both including the linear viscous damping terms into the Narimanov–Moiseev-type nonlinear multimodal theory of Part 1 and carrying out the corresponding steady-state resonant sloshing analysis.

By writing the present paper, we suggest the three following generalisations of Part 1 in mind. First, the steady-state undamped sloshing analysis is extended to the case of an arbitrary horizontal oblique harmonic excitation. This includes constructing an analytical periodic solution of the Narimanov–Moiseev-type modal system and studying its stability. What happens with the effective frequency ranges for the stable steady-state wave regimes and the corresponding response curves is examined versus the forcing direction, which changes from longitudinal to diagonal one. Secondly, we introduce the linear damping terms in the asymptotic modal system and study how this may change the steady-state resonant sloshing. We show that the linear damping leads to a qualitatively other steady-state resonant sloshing and prove that (i′)–(iii′) can replace (i)–(iii). According to our asymptotic theory, this happens when the introduced damping coefficients in the governing equations of the primary excited sloshing modes are of $O(\eta^{2/3})$. Such a damped sloshing is relevant for a relatively small laboratory tank (Ducci & Weheliye 2014). The results can also be useful, e.g. for modelling the sloshing effect in the tetra-pack-type cardboard cartons that are filled by a Newtonian liquid (milk, juice, etc.) in the packing machines (Grundelius 2001). Thirdly, we study a complex (double) effect of the linear damping and the forcing direction on the steady-state response curves. Even though the numerical examples were done for the liquid depth-to-tank width ratio $h/L = 0.6$, the results should be qualitatively the same for $0.5 \lesssim h/L$ since the hydrodynamic coefficients in the Narimanov–Moiseev-type modal system weakly change for these depths. These steady-state results are compared with the measured maximum wave

https://doi.org/10.1017/jfm.2017.263 Published online by Cambridge University Press

elevations by Ikeda *et al.* (2012). Even though our analytical study can evaluate the phase lags between the harmonic forcing signal as well as between the Stokes cross-wave components, the analysis of these lags is not reported. The analysis deserves an independent publication, especially, in the context of the angular steady flow phenomenon (V-vortex), which was reported by Royon-Lebeaud, Hopfinger & Cartellier (2007) for swirling.

In § 2, we introduce preliminaries from Part 1 and write down the nine-dimensional Narimanov–Moiseev-type system of ordinary differential (modal) equations, which are equipped with the linear damping terms associated with the logarithmic decrement of the corresponding natural sloshing modes. An oblique harmonic horizontal tank forcing is considered. Utilising the modal equations suggests a set of asymptotic relations between the non-dimensional input parameters on the $\epsilon = O(\eta)$ scale. Accounting for the linear damping in these equations requires the damping coefficients (rates) satisfying the corresponding asymptotic conditions in terms of η.

Can the latter asymptotic conditions be satisfied for realistic model tests? This query is answered in § 3. We utilise the modified Keulegan's formula by Faltinsen & Timokha (2009, (6.140)) to estimate the damping ratios caused by the linear laminar boundary layer on the wetted tank surface. The formula provides the lowest-order asymptotic approximation in terms of the small parameter $\sqrt{\nu T_{i,j}/L^2}$ (ν is the kinematic viscosity and $T_{i,j}$ is the natural period of the i, j-mode). Computations for the tap water at 20 °C show that the theoretical non-dimensional damping coefficients have similar order for the nine lowest natural sloshing modes (governed by the multimodal equations). Because the theoretical damping ratios increase with decreasing L, the required asymptotic condition for the non-dimensional damping coefficients cannot be satisfied for larger containers, as in the experiments of Part 1 ($L = 1$ m). For the laboratory tests by Ikeda *et al.* (2012) with the relatively small 0.1×0.1 m base container, one should recall the experimental results by Keulegan (1959) and Henderson & Miles (1994) (see also discussion in pp. 264–265 by Faltinsen & Timokha 2009) who pointed out that the linear boundary-layer estimate by Faltinsen & Timokha (2009, (6.140)) gives only a lower bound of the linear damping ratios for $L \lesssim 0.2$ m. The difference between the theoretical and measured values can be significant so that, for instance, the computed non-dimensional damping coefficient for the first natural sloshing mode in the 0.1×0.1 m tank is equal to 0.01 while Ikeda *et al.* (2012) measured it to be approximately 0.0256. The latter value can be assumed to be of the required $O(\eta^{2/3})$ in the model tests by Ikeda *et al.* (2012) where $\eta \approx 0.0075$.

An asymptotic steady-state (periodic) solution of the nonlinear Narimanov–Moiseev-type multimodal system with linear damping terms is analytically derived in § 4 for an arbitrary oblique harmonic forcing. The derivation leads to a secular (solvability) system of nonlinear algebraic equations, which couples the four lowest-order, $O(\eta^{1/3})$, amplitude parameters. The multitiming technique from Part 1 is generalised to study stability of the derived steady-state solution. Part 1 shows how to get an analytical solution of the secular system with the zero damping terms for both longitudinal and diagonal excitations. This analytical scheme is, in our opinion, not applicable for the oblique forcing and/or the non-zero damping.

Because the linear damping causes the two phase lags ψ and φ for the two lowest-order periodic sloshing components (the components are associated with the perpendicular Stokes modes), a more physically relevant form of the secular equations, which couples the two amplitudes A, B and the pair ψ, φ for the two Stokes modes, is needed. Such a secular system is derived in § 5. We show that the steady-state

https://doi.org/10.1017/jfm.2017.263 Published online by Cambridge University Press

resonant sloshing implies a standing wave if and only if $\sin(\varphi - \psi) = 0$. Furthermore, we construct an analytical solution of the new secular equations for the undamped case and an arbitrary (oblique) forcing direction. The solution shows that the oblique forcing theoretically causes maximum six different standing resonant waves and up to three different swirling modes for a fixed forcing frequency. Each swirling mode implies two physically identical angularly progressive waves in clockwise and counterclockwise directions, respectively.

The authors do not know how to construct an analytical solution of the secular equations for the damped resonant sloshing, except for the longitudinal forcing (this solution is derived and presented). However, without such a solution and extensive numerical experiments, we prove in § 5.3 a series of specific qualitative properties regarding the secular equations, which make it possible to confirm that (i′)–(iii′) indeed replace (i)–(iii) when damping matters. An important conclusion is that the damped sloshing formally makes impossible the square-like regime and any other standing resonant waves. However, because the standing wave criterion admits an asymptotic interpretation, $\sin(\varphi - \psi) = O(\eta^{1/3})$, one can introduce an almost standing wave mode for certain input parameters. This occurs when one from the two modified Stokes modes, which constitute swirling, has an asymptotically dominant character. These waves were discovered in the experiments by Ikeda *et al.* (2012, figure 4).

In § 6, we conduct a set of computations to examine the evolution of the undamped and damped response curves versus the angle $0 \leqslant \gamma \leqslant \pi/4$ between the excitation direction and the Ox axis ($\gamma = 0$ corresponds to the longitudinal forcing). The branching for the damped case is similar to that by Ikeda *et al.* (2012) who adopted another adaptive-type modal equations. Difference between damped and undamped branchings can be significant for the oblique (diagonal) forcing. However, the frequency ranges, where all the steady-state wave regimes are unstable and irregular motions occur, undergo insignificant changes. The damping significantly influences the branching for swirling.

In § 7, we compare our theoretical predictions of the maximum wave elevations (the damped sloshing) with experimental measurements by Ikeda *et al.* (2012). The agreement looks rather favourable except, probably, for the larger-amplitude swirling mode. The latter discrepancy can be lowered by adopting a speculatively larger damping ratios as it was done by Ikeda *et al.* (2012).

2. Statement of the problem

We follow Part 1 and consider a rigid square-base tank, which is partially filled with an incompressible liquid to a mean liquid depth h. The tank oscillates harmonically and horizontally by surge $\eta_1(t) = L\eta_{1a}\cos(\sigma t)$ and sway $\eta_2(t) = L\eta_{2a}\cos(\sigma t)$, where L is the square base side and the non-dimensional forcing amplitudes are small and associated with a small input parameter $\epsilon \sim \eta$, i.e.

$$\sqrt{\eta_{1a}^2 + \eta_{2a}^2} = \eta = O(\epsilon) \ll 1. \tag{2.1}$$

The liquid motions are considered in the tank-fixed coordinate system $Oxyz$ so that the mean free surface Σ_0 belongs to the Oxy plane and Oz passes through the centre of Σ_0 (figure 1). The free surface $\Sigma(t) : z = f(x, y, t)$ and the absolute velocity potential $\Phi(x, y, z, t)$ must simultaneously be found from the corresponding free-surface problem or its variational analogy (see, chap. 2, 7 and 9 by Faltinsen & Timokha 2009). The steady-state resonant waves are described by solutions which satisfy the periodicity condition $f(x, y, t + 2\pi/\sigma) = f(x, y, t)$ and $\Phi(x, y, z, t + 2\pi/\sigma) = \Phi(x, y, z, t)$.

https://doi.org/10.1017/jfm.2017.263 Published online by Cambridge University Press

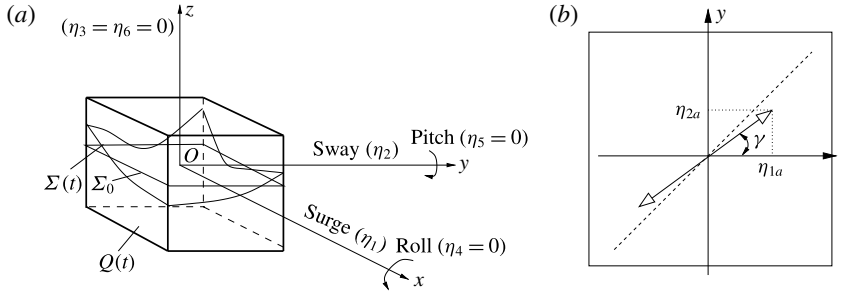


FIGURE 1. The horizontally excited tank in (*a*). (*b*) Shows the excitation direction with the non-dimensional forcing amplitude $\eta = \sqrt{\eta_{1a}^2 + \eta_{2a}^2}$ whose projections on the coordinate axes are $\eta_{1a} = \eta\cos\gamma$ and $\eta_{2a} = \eta\sin\gamma$, $0 \leqslant \gamma \leqslant \pi/4$.

Furthermore, the forcing frequency σ is close to the lowest natural sloshing frequency $\sigma_1 = \sigma_{0,1} = \sigma_{1,0}$ (which corresponds to the two longest Stokes cross-waves) taken from the infinite set

$$\sigma_{i,j}^2 = \frac{g\pi}{L}\sqrt{i^2 + j^2}\tanh\left(\frac{\pi\sqrt{i^2 + j^2}\,h}{L}\right) \tag{2.2}$$

(chap. 4 by Faltinsen & Timokha 2009).

To get a non-dimensional formulation, we adopt the characteristic size L and the characteristic time $1/\sigma_1$. This implies, in particular, the unit breadth = width for the non-dimensional tank and the normalised natural sloshing frequencies and the forcing frequency are

$$\bar{\sigma}_{i,j} = \frac{\sigma_{i,j}}{\sigma_1} \quad \text{and} \quad \bar{\sigma} = \frac{\sigma}{\sigma_1}, \tag{2.3a,b}$$

respectively.

Adopting the nonlinear multimodal method for the non-dimensional sloshing problem suggests the Fourier presentation of the free surface

$$z = f(x, y, t) = \sum_{i,j \geqslant 0, i+j \neq 0} \beta_{i,j}(t)(f_i^{(1)}(x) f_j^{(2)}(y)), \tag{2.4}$$

where $(f_i^{(1)}(x) f_j^{(2)}(y))$ are the non-dimensional natural sloshing modes,

$$f_i^{(1)}(x) = \cos\left(\pi i\left(x + \tfrac{1}{2}\right)\right), \quad f_i^{(2)}(y) = \cos\left(\pi i\left(y + \tfrac{1}{2}\right)\right), \quad i \geqslant 0, \tag{2.5a,b}$$

corresponding to the natural sloshing frequencies (2.2) and $\beta_{i,j}(t)$ are the sloshing-related generalised coordinates.

Part 1 derived the Narimanov–Moiseev-type nonlinear (asymptotic) modal system coupling $\beta_{i,j}(t)$, which takes, after re-denoting $\beta_{1,0} = a_1$, $\beta_{2,0} = a_2$, $\beta_{0,1} = b_1$, $\beta_{0,2} = b_2$, $\beta_{1,1} = c_1$, $\beta_{3,0} = a_3$, $\beta_{2,1} = c_{21}$, $\beta_{1,2} = c_{12}$, $\beta_{0,3} = b_3$, the form

$$\ddot{a}_1 + \boxed{2\xi_{1,0}\dot{a}_1} + a_1 + d_1(\ddot{a}_1 a_2 + \dot{a}_1\dot{a}_2) + d_2(\ddot{a}_1 a_1^2 + \dot{a}_1^2 a_1) + d_3\ddot{a}_2 a_1 + d_6\ddot{a}_1 b_1^2 + d_9\ddot{c}_1 b_1$$
$$+ \ddot{b}_1(d_7 c_1 + d_8 a_1 b_1) + d_{10}\dot{b}_1^2 a_1 + d_{11}\dot{a}_1\dot{b}_1 b_1 + d_{12}\dot{b}_1\dot{c}_1 = P_{1,0}\eta_{1a}\bar{\sigma}^2\cos(\bar{\sigma}t), \tag{2.6a}$$

https://doi.org/10.1017/jfm.2017.263 Published online by Cambridge University Press

$$\ddot{b}_1 + \boxed{2\xi_{0,1}\dot{b}_1} + b_1 + d_1(\ddot{b}_1 b_2 + \dot{b}_1\dot{b}_2) + d_2(\ddot{b}_1 b_1^2 + \dot{b}_1^2 b_1) + d_3\ddot{b}_2 b_1 + d_6\ddot{b}_1 a_1^2 + d_9\ddot{c}_1 a_1 + \ddot{a}_1(d_7 c_1 + d_8 a_1 b_1) + d_{10}\dot{a}_1^2 b_1 + d_{11}\dot{a}_1\dot{b}_1 a_1 + d_{12}\dot{a}_1\dot{c}_1 = P_{0,1}\eta_{2a}\bar{\sigma}^2\cos(\bar{\sigma}t), \tag{2.6b}$$

$$\ddot{a}_2 + \boxed{2\xi_{2,0}\bar{\sigma}_{0,2}\dot{a}_2} + \bar{\sigma}_{2,0}^2 a_2 + d_4\ddot{a}_1 a_1 + d_5\dot{a}_1^2 = 0; \tag{2.6c}$$

$$\ddot{b}_2 + \boxed{2\xi_{0,2}\bar{\sigma}_{0,2}\dot{b}_2} + \bar{\sigma}_{0,2}^2 b_2 + d_4\ddot{b}_1 b_1 + d_5\dot{b}_1^2 = 0, \tag{2.6d}$$

$$\ddot{c}_1 + \boxed{2\xi_{1,1}\bar{\sigma}_{1,1}\dot{c}_1} + \bar{\sigma}_{1,1}^2 c_1 + \hat{d}_1\ddot{a}_1 b_1 + \hat{d}_2\ddot{b}_1 a_1 + \hat{d}_3\dot{a}_1\dot{b}_1 = 0, \tag{2.6e}$$

$$\ddot{a}_3 + \boxed{2\xi_{3,0}\bar{\sigma}_{3,0}\dot{a}_3} + \bar{\sigma}_{3,0}^2 a_3 + \ddot{a}_1(q_1 a_2 + q_2 a_1^2) + q_3\ddot{a}_2 a_1 + q_4\dot{a}_1^2 a_1 + q_5\dot{a}_1\dot{a}_2 = P_{3,0}\eta_{1a}\bar{\sigma}^2\cos(\bar{\sigma}t), \tag{2.7a}$$

$$\ddot{c}_{21} + \boxed{2\xi_{2,1}\bar{\sigma}_{2,1}\dot{b}_3} + \bar{\sigma}_{2,1}^2 c_{21} + \ddot{a}_1(q_6 c_1 + q_7 a_1 b_1) + \ddot{b}_1(q_8 a_2 + q_9 a_1^2) + q_{10}\ddot{a}_2 b_1 + q_{11}\ddot{c}_1 a_1 + q_{12}\dot{a}_1^2 b_1 + q_{13}\dot{a}_1\dot{b}_1 a_1 + q_{14}\dot{a}_1\dot{c}_1 + q_{15}\dot{a}_2\dot{b}_1 = 0, \tag{2.7b}$$

$$\ddot{c}_{12} + \boxed{2\xi_{1,2}\bar{\sigma}_{1,2}\dot{b}_3} + \bar{\sigma}_{1,2}^2 c_{12} + \ddot{b}_1(q_6 c_1 + q_7 a_1 b_1) + \ddot{a}_1(q_8 b_2 + q_9 b_1^2) + q_{10}\ddot{b}_2 a_1 + q_{11}\ddot{c}_1 b_1 + q_{12}\dot{b}_1^2 a_1 + q_{13}\dot{a}_1\dot{b}_1 b_1 + q_{14}\dot{b}_1\dot{c}_1 + q_{15}\dot{a}_1\dot{b}_2 = 0, \tag{2.7c}$$

$$\ddot{b}_3 + \boxed{2\xi_{0,3}\bar{\sigma}_{0,3}\dot{b}_3} + \bar{\sigma}_{0,3}^2 b_3 + \ddot{b}_1(q_1 b_2 + q_2 b_1^2) + q_3\ddot{b}_2 b_1 + q_4\dot{b}_1^2 b_1 + q_5\dot{b}_1\dot{b}_2 = P_{0,3}\eta_{2a}\bar{\sigma}^2\cos(\bar{\sigma}t); \tag{2.7d}$$

where

$$P_{i,0} = P_{0,i} = \frac{2}{\pi i}[(-1)^i - 1]\tanh(\pi i h/L), \tag{2.8}$$

Part 1 also gives explicit expressions for the hydrodynamic coefficients at the nonlinear terms, which are also computed in Faltinsen & Timokha (2009, tables 9.1–9.2).

The derivation details and applicability limits of the nonlinear asymptotic modal system (2.6)–(2.7) are extensively discussed in Part 1. The system requires that (i) the non-dimensional forcing amplitude is small, (ii) the forcing frequency σ is close to the lowest natural sloshing frequency σ_1 ($\bar{\sigma}$ satisfies the Moiseev detuning), (iii) the two lowest perpendicular Stokes modes (associated with the generalised coordinates $a_1(t)$ and $b_1(t)$) give the lowest-order (dominant) asymptotic contribution $O(\eta^{1/3}) = O(\epsilon^{1/3})$ and (iv) there are no secondary resonances.

The actual asymptotic ordering of the higher sloshing modes (generalised coordinates) are mathematically deduced following the Narimanov–Moiseev asymptotic technique, which proves that the second-order modes are exclusively associated with a_2, b_2 and c_1 but c_{12}, c_{21}, a_3 and b_3 are of the third order on the $\epsilon = O(\eta) \ll 1$ scale. The Narimanov–Moiseev-type modal system may fail with decreasing the liquid depth, increasing the forcing amplitude and for the transient sloshing. Physically, this is due to the secondary resonance phenomenon. The multimodal analysis needs then the so-called adaptive ordering whose concept was elaborated by Faltinsen *et al.* (2005*b*), Faltinsen, Rognebakke & Timokha (2006*b*). In the corresponding adaptive modal systems, the higher-order generalised coordinates, including a_2, b_2, c_1 and c_{12}, c_{21}, a_3, b_3 as well as generalised coordinates, which are not accounted for by

https://doi.org/10.1017/jfm.2017.263 Published online by Cambridge University Press

the Narimanov–Moiseev asymptotic scheme, can contribute to the lower asymptotic components. A version of the adaptive modal ordering was adopted by Ikeda *et al.* (2012), probably to improve agreement with experiments for transients; they used a direct simulation of transient and steady-state waves (combined with a path-following procedure) to numerically analyse the steady-state regimes and their stability.

For the oblique forcing in figure 1(*b*), the assumptions (i–iv) can be mathematically formalised as

$$\eta_{2a} = \delta\eta_{1a}, \quad 0 \leqslant \delta = \tan\gamma \leqslant 1; \quad 0 < \epsilon = P_1\eta_{1a} = -P_{1,0}\eta_{1a} = O(\eta), \tag{2.9a–c}$$

$$\Lambda = (\sigma_1/\sigma)^2 - 1 = \bar{\sigma}^{-2} - 1 = O(\epsilon^{2/3}) \quad \text{(the Moiseev detuning)}, \tag{2.9d}$$

$$a_1 \sim b_1 = O(\epsilon^{1/3}) \quad \Rightarrow \quad a_2 \sim b_2 \sim c_1 = O(\epsilon^{2/3}) \quad a_3 \sim b_3 \sim c_{21} \sim c_{12} = O(\epsilon), \tag{2.9e}$$

$$\bar{\sigma}_{0,2}^2 - 4 = O(1), \quad \bar{\sigma}_{1,1}^2 - 4 = O(1), \quad \bar{\sigma}_{0,3}^2 - 9 = O(1), \quad \bar{\sigma}_{1,2}^2 - 9 = O(1). \tag{2.9f–i}$$

3. Linear viscous damping ratios

Because (2.6)–(2.7) suggests neglecting the $O(\epsilon)$ terms, the non-dimensional damping coefficients of the linear framed terms should possess the asymptotic conditions

$$2\xi_{1,0} = 2\xi_{0,1} = O(\epsilon^{2/3}); \quad 2\xi_{i,j}\bar{\sigma}_{i,j} = O(\epsilon^{1/3}), \quad i+j=2; \quad 2\xi_{i,j}\bar{\sigma}_{i,j} = O(1), \quad i+j=3 \tag{3.1a–c}$$

to be accounted for simultaneously. Because a_1 and b_1 have a dominant character, one should concentrate on

$$\xi = 2\xi_{1,0} = O(\epsilon^{2/3}) \tag{3.2}$$

for the lowest-order Stokes modes governed by (2.6).

The linear damping for sloshing in a clean tank is extensively discussed in Faltinsen & Timokha (2009, chap. 6). The damping ratios $\xi_{i,j}$ are associated with the logarithmic decrements of the natural sloshing modes whose primary contribution is caused by the linear boundary layer at the wetted tank surface. Faltinsen & Timokha (2009, (6.140)) gives the asymptotic approximation

$$\xi_{i,j} = \sqrt{\frac{\nu}{2L^2\sigma_{i,j}}}\left[3 + 2\pi\frac{\sqrt{i^2+j^2}(0.5 - h/L)}{\sinh(2\pi\sqrt{i^2+j^2}\,h/L)}\right] \tag{3.3}$$

in terms of $\sqrt{\nu/(2L^2\sigma_{i,j})} \ll 1$, where ν is the kinematic viscosity coefficient. As discussed by Keulegan (1959) and Faltinsen & Timokha (2009, § 6.3.1), (3.3) provides a rather accurate estimate of the damping ratios for the lower natural sloshing modes in a relatively large rectangular tank. When $L \lesssim 0.2$ m, the experimental damping ratios may be larger than this theoretical value. Keulegan (1959) explained this fact by the dynamic contact angle (meniscus) effect. He illustrated his hypothesis by comparing the damping ratios for Lucite and glass basins (see, figure 6.6 by Faltinsen & Timokha 2009), which are clearly different and larger than the estimate (3.3). The higher experimental damping ratios for the relatively small tanks were described by Henderson & Miles (1994) and Ikeda *et al.* (2012) ($L = 0.1$ m and $h/L = 0.6$). Ikeda *et al.* (2012) reported the experimental value $\xi = 2 \times 0.0128 = 0.0256$ while (3.3) computes $\xi = 2\xi_{1,0} = 0.01$.

https://doi.org/10.1017/jfm.2017.263 Published online by Cambridge University Press

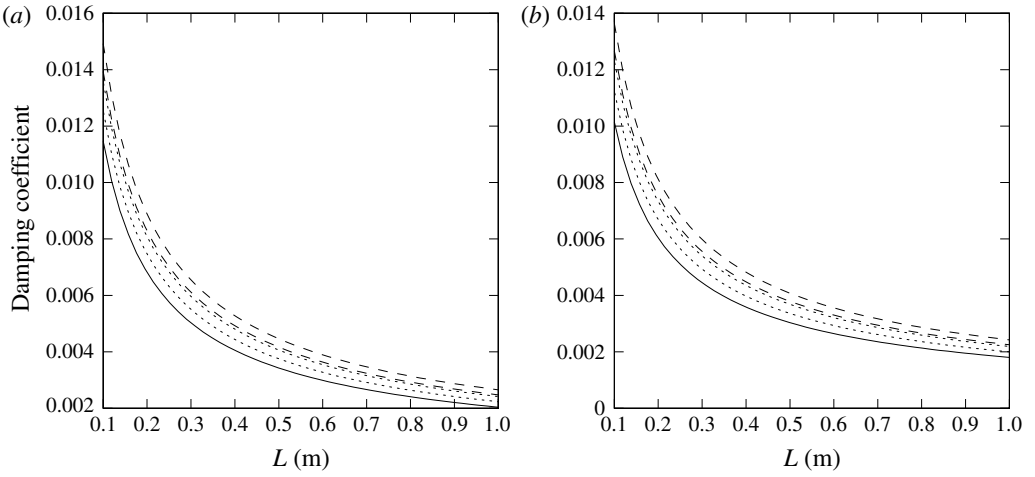


FIGURE 2. The theoretical non-dimensional damping coefficients $2\xi_{i,j}\bar{\sigma}_{i,j}$ in the framed terms of the modal equations (2.6)–(2.7) versus the tank breadth = width L (m). The values are computed by (3.3) for tap water with $\nu = 10^{-6}$ (m^2 s^{-1}). The solid line corresponds to $\xi = 2\xi_{0,1} = 2\xi_{1,0}$, the dotted lines imply $2\xi_{2,0}\bar{\sigma}_{2,0}$ and $2\xi_{1,1}\bar{\sigma}_{1,1}$ and the dashed lines are used to mark $2\xi_{3,0}\bar{\sigma}_{3,0}$ and $2\xi_{2,1}\bar{\sigma}_{2,1}$. Panel (*a*) is drawn for $h/L = 0.35$ and (*b*) is for $h/L = 0.6$. The damping coefficients have the asymptotic $L^{-3/4}$.

The non-dimensional damping coefficients $2\xi_{i,j}\bar{\sigma}_{i,j}$ for tap water with $\nu = 10^{-6}$ m^2 s^{-1} are computed in figure 2 versus the tank breadth = width L (m) for $h/L = 0.35$ and 0.6. The solid lines correspond to $\xi = 2\xi_{0,1} = 2\xi_{1,0}$, the dotted lines imply $2\xi_{2,0}\bar{\sigma}_{2,0}$ and $2\xi_{1,1}\bar{\sigma}_{1,1}$ and the dashed lines are used to mark $2\xi_{3,0}\bar{\sigma}_{3,0}$ and $2\xi_{2,1}\bar{\sigma}_{2,1}$. The figure shows that the relative difference between these lines is not large and the computed non-dimensional damping coefficients for the considered nine sloshing modes have similar asymptotic order. As a consequence, (3.1) cannot be satisfied for all damping coefficients. One should focus on (3.2) for a_1 and b_1, but neglect the linear damping terms for the higher-order generalised coordinates in (2.6*c*)–(2.7).

In Part 1 and Ikeda *et al.* (2012), the non-dimensional experimental amplitudes were approximately $O(\epsilon) = \eta = 0.0075$ (actually, 0.0078 and 0.00725). The first tank has the horizontal dimension $L = 1$ m. For this size, (3.3) provides a rather accurate prediction of ξ. Figure 2 shows that $\xi = 0.002 < \eta$ in this case so that the asymptotic condition (3.2) is clearly not satisfied. For the laboratory tank ($L = 0.1$ m) by Ikeda *et al.* (2012), the theoretical damping coefficient is $\xi = 0.01$ but the authors reported the experimental $\xi = 0.0256$. This value may theoretically be considered as satisfying (3.2) for $\eta = 0.0075$.

4. Steady-state asymptotic solution and its stability

By applying the analytical scheme by Faltinsen *et al.* (2003, § 3.2), one can derive an exact asymptotic steady-state solution of (2.6)–(2.7) starting with

$$a_1(t) = a\cos\bar{\sigma}t + \bar{a}\sin\bar{\sigma}t + O(\epsilon^{1/3}); \quad b_1(t) = \bar{b}\cos\bar{\sigma}t + b\sin\bar{\sigma}t + O(\epsilon^{1/3}), \quad (4.1a,b)$$

which determines the lowest-order approximation of the surface wave

$$z = S(x, y; a, \bar{b})\cos\bar{\sigma}t + S(x, y; \bar{a}, b)\sin\bar{\sigma}t + O(\epsilon^{1/3}), \quad (4.2)$$

where $S(x, y; a, b) = af_1^{(1)}(x) + bf_1^{(2)}(y)$ is the combined Stokes mode.

https://doi.org/10.1017/jfm.2017.263 Published online by Cambridge University Press

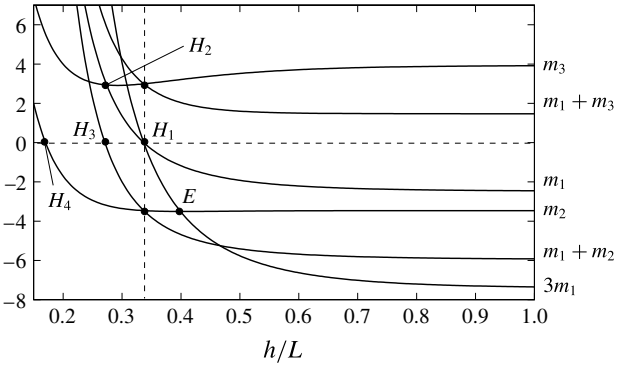


FIGURE 3. Reprint from Faltinsen *et al.* (2003, figure 4) illustrating the non-dimensional coefficients $m_i(h/L)$, $i = 1, 2, 3$ and their linear combinations versus the liquid-depth-to-breadth ratio h/L for a square-base basin. The point H_1 ($m_1 = 0$, $h/L = 0.337\ldots$) denotes the soft/hard spring change for the planar steady-state waves. The point H_2 ($m_1 = m_3$) defines $h/L = 0.274\ldots$, H_3 implies $h/L = 0.27\ldots$, where $m_1 + m_2 = 0$, and H_4 corresponds to $h/L = 0.17\ldots$, where $m_2 = 0$. The point E ($h/L = 0.4\ldots$) is obtained from the equality $m_2 = 3m_1$.

The derivation is presented in appendix A. The asymptotic procedure is almost identical to that from Part 1. We neglect the linear damping terms in (2.6*c*) (see, discussion in § 3). The third-order generalised coordinates by (2.7) are driven. They do not affect a_1, b_1, a_2, b_2 and c_1. There is the necessary solvability condition appearing as the (secular) system of nonlinear algebraic equations

$$\left.\begin{aligned}
&①:\ a[\Lambda + m_1(a^2 + \bar{a}^2) + m_2\bar{b}^2 + m_3 b^2] + \bar{a}[(m_2 - m_3)\bar{b}b + \xi] = \epsilon,\\
&②:\ \bar{a}[\Lambda + m_1(a^2 + \bar{a}^2) + m_2 b^2 + m_3\bar{b}^2] + a[(m_2 - m_3)\bar{b}b - \xi] = 0,\\
&③:\ b[\Lambda + m_1(b^2 + \bar{b}^2) + m_2\bar{a}^2 + m_3 a^2] + \bar{b}[(m_2 - m_3)\bar{a}a - \xi] = 0,\\
&④:\ \bar{b}[\Lambda + m_1(b^2 + \bar{b}^2) + m_2 a^2 + m_3\bar{a}^2] + b[(m_2 - m_3)\bar{a}a + \xi] = \delta\epsilon,
\end{aligned}\right\} \tag{4.3}$$

which couples the non-dimensional amplitude parameters $a, \bar{a}, b$ and $\bar{b}$. The right-hand side components are defined by (2.9*a*–*c*). The coefficients m_1 and m_3 are strongly affected by the second-order generalised coordinates by (2.6*c*), so that

$$\left.\begin{aligned}
m_1 &= -\tfrac{1}{2}d_2 - d_1\left(p_0 - \tfrac{1}{2}h_0\right) - 2h_0 d_3,\\
m_2 &= -\tfrac{3}{4}d_6 + \tfrac{1}{4}d_{10} - \tfrac{3}{4}d_8 + \tfrac{1}{4}d_{11} - d_7 p_1 - h_1\left(\tfrac{1}{2}d_7 + 2d_9 - d_{12}\right),\\
m_3 &= -\tfrac{1}{4}d_6 + \tfrac{3}{4}d_{10} - \tfrac{1}{4}d_8 - \tfrac{1}{4}d_{11} - h_1\left(\tfrac{1}{2}d_7 + 2d_9 - d_{12}\right)
\end{aligned}\right\} \tag{4.4}$$

and $\xi = 2\xi_{0,1} = 2\xi_{1,0}$, which are functions of the non-dimensional liquid depth h/L. Owing to (2.9*d*) and (3.2), all quantities in (4.3) have the same asymptotic order $O(\epsilon)$. The functions $m_i = m_i(h/L)$ were analysed in Part 1 (see, figure 3). The graphs show that $m_2 < 0$, $h/L > 0.17, \ldots$, $m_1 + m_2 < 0$ for $h/L > 0.27\ldots$ and $m_2 - m_3 < 0$, $m_1 + m_3 > 0$ for the finite liquid depths, $0.5 \lesssim h/L$. We use these inequalities in our forthcoming analytical and numerical studies and, therefore, these are, generally speaking, restricted to $0.5 \lesssim h/L$.

We can use the linear Lyapunov method and the multitiming technique to study the stability of the constructed asymptotic steady-state solutions. For this purpose, we

https://doi.org/10.1017/jfm.2017.263 Published online by Cambridge University Press

introduce the slowly varying time $\tau = (\epsilon^{2/3}\bar{\sigma}t)/2$, whose order is chosen according to the Moiseyev detuning $\bar{\sigma}^{-2} - 1 = O(\epsilon^{2/3})$, and express the perturbed solutions as

$$\left.\begin{aligned} a_1 &= (a + \alpha(\tau))\cos\bar{\sigma}t + (\bar{a} + \bar{\alpha}(\tau))\sin\bar{\sigma}t + O(\epsilon^{1/3}),\\ b_1 &= (\bar{b} + \bar{\beta}(\tau))\cos\bar{\sigma}t + (b + \beta(\tau))\sin\bar{\sigma}t + O(\epsilon^{1/3}), \end{aligned}\right\} \tag{4.5}$$

where a, $\bar{a}$, b and $\bar{b}$ come from (4.3). Inserting (4.5) into (2.6)–(2.7), gathering terms of the lowest asymptotic quantities order and keeping linear terms in α, $\bar{\alpha}$, β and $\bar{\beta}$ lead to the following linear system of ordinary differential equations

$$\boldsymbol{s}' + \xi\boldsymbol{s} + \boldsymbol{S}\boldsymbol{s} = 0, \tag{4.6}$$

where $\boldsymbol{s} = (\alpha, \bar{\alpha}, \beta, \bar{\beta})^{\mathrm{T}}$, the prime is the differentiation by τ, and the matrix $\boldsymbol{S}$ has the following elements

$$\left.\begin{aligned} s_{11} &= -2m_1a\bar{a} - (m_2 - m_3)b\bar{b}; \quad s_{12} = -\Lambda - m_1a^2 - 3m_1\bar{a}^2 - m_2b^2 - m_3\bar{b}^2,\\ s_{13} &= -2m_2\bar{a}b - (m_2 - m_3)a\bar{b}; \quad s_{14} = -2m_3\bar{a}\bar{b} - (m_2 - m_3)ab,\\ s_{21} &= \Lambda + 3m_1a^2 + m_1\bar{a}^2 + m_2\bar{b}^2 + m_3b^2; \quad s_{22} = 2m_1a\bar{a} + (m_2 - m_3)b\bar{b},\\ s_{23} &= 2m_3ab + (m_2 - m_3)\bar{a}\bar{b}; \quad s_{24} = 2m_2a\bar{b} + (m_2 - m_3)\bar{a}b,\\ s_{31} &= 2m_2a\bar{b} + (m_2 - m_3)b\bar{a}; \quad s_{32} = 2m_3\bar{a}\bar{b} + (m_2 - m_3)ab,\\ s_{33} &= 2m_1b\bar{b} + (m_2 - m_3)a\bar{a}; \quad s_{34} = \Lambda + m_1b^2 + 3m_1\bar{b}^2 + m_2a^2 + m_3\bar{a}^2,\\ s_{41} &= -2m_3ab - (m_2 - m_3)\bar{a}\bar{b}; \quad s_{42} = -2m_2\bar{a}b - (m_2 - m_3)a\bar{b},\\ s_{43} &= -\Lambda - 3m_1b^2 - m_1\bar{b}^2 - m_2\bar{a}^2 - m_3a^2; \quad s_{44} = -2m_1b\bar{b} - (m_2 - m_3)a\bar{a}. \end{aligned}\right\} \tag{4.7}$$

The fundamental solution $\boldsymbol{s} = \exp(\lambda\tau)\boldsymbol{a}$ of (4.6) follows from the spectral matrix problem $[(\lambda + \xi)E + S]\boldsymbol{a} = 0$, where λ are the unknown eigenvalues and $\boldsymbol{a}$ are the corresponding eigenvectors. Computations give the following characteristic bi-quadratic equation

$$(\lambda + \xi)^4 + s_1(\lambda + \xi)^2 + s_0 = 0, \tag{4.8}$$

where s_0 is the determinant of $\boldsymbol{S}$ and s_1 is a complicated function of the elements of $\boldsymbol{S}$. The eigenvalues λ can be expressed as $-\xi \pm \sqrt{x_{1,2}}$, where $x_{1,2} = (-s_1 \pm \sqrt{s_1^2 - 4s_0})/2$ are two solutions of the quadratic equation $x^2 + s_1x + s_0 = 0$. The fixed-point solution (associated with a, $\bar{a}$, b and $\bar{b}$) is asymptotically stable (α, $\bar{\alpha}$, β and $\bar{\beta}$ exponentially decay with τ) if and only if the real component of λ is strongly negative.

In the limit case $\xi \to 0$, Part 1 derived the stability condition ($\Re[\lambda] < 0$) in the following form

$$s_1^2 - 4s_0 \geqslant 0 \quad s_0 \geqslant 0 \quad s_1 \geqslant 0. \tag{4.9}$$

For $O(\epsilon^{2/3}) = \xi > 0$, the stability condition can be written as the alternative

$$\left.\begin{aligned} &\text{either} \quad s_1^2 - 4s_0 \geqslant 0 \quad \text{and} \quad -s_1 + \sqrt{s_1^2 - 4c_s} \leqslant 0 \quad (\Leftrightarrow s_0 \geqslant 0 \text{ and } s_1 \geqslant 0),\\ &\text{or } s_1^2 - 4s_0 \geqslant 0 \quad \text{and} \quad -s_1 + \sqrt{s_1^2 - 4s_0} > 0 \quad \text{and} \quad \sqrt{\tfrac{1}{2}\left(-s_1 + \sqrt{s_1^2 - 4s_0}\right)} < \xi,\\ &\qquad\qquad \text{or} \quad s_1^2 - 4s_0 < 0 \quad \text{and} \quad \sqrt{2\sqrt{s_0} - s_1} < \xi. \end{aligned}\right\} \tag{4.10}$$

Part 1 constructed an analytical solution of (4.3) for the undamped sloshing with $\xi = 0$ and either longitudinal ($\delta = 0$) or diagonal ($\delta = 1$) excitation. The proposed analytical technique is most probably not applicable for oblique forcing directions with $0 < \delta < 1$ as well as for the damped case with $\xi = O(\epsilon^{2/3})$. The forthcoming section proposes an alternative analytical approach.

https://doi.org/10.1017/jfm.2017.263 Published online by Cambridge University Press

5. Damped versus undamped sloshing: qualitative differences

5.1. *Rewriting (4.3) in an alternative form*

The non-zero linear damping naturally leads the two phase lags, ψ and φ, for the two perpendicular Stokes modes $f_1^{(1)}(x)$ and $f_1^{(2)}(y)$ (along the Ox and Oy directions) in (4.2), which are characterised by the lowest-order amplitude parameters $a, \bar{a}$ and $b, \bar{b}$, respectively. A physically relevant form of (4.3) should therefore couple the 'integral' lowest-order amplitudes A, B and the phase lags ψ, φ:

$$A=\sqrt{a^2+\bar{a}^2} \quad \text{and} \quad B=\sqrt{\bar{b}^2+b^2}>0, \tag{5.1a,b}$$

$$a=A\cos\psi, \quad \bar{a}=A\sin\psi, \quad \bar{b}=B\cos\varphi, \quad b=B\sin\varphi. \tag{5.1c–f}$$

To get these equations, we insert (5.1) into expressions $\bar{a}\,①-a\,②$, $\bar{b}\,③-b\,④$, $a\,①+\bar{a}\,②$ and $b\,③+\bar{b}\,④$ of (4.3), which give

$$\left.\begin{aligned} \boxed{1}:\, A\,[\Lambda+m_1A^2+\mathcal{F}B^2]=\epsilon\cos\psi, \quad \boxed{3}:\, A\,[\mathcal{D}B^2+\xi]=\epsilon\sin\psi,\\ \boxed{2}:\, B\,[\Lambda+m_1B^2+\mathcal{F}A^2]=\delta\epsilon\cos\varphi, \quad \boxed{4}:\, B\,[\mathcal{D}A^2-\xi]=-\delta\epsilon\sin\varphi, \end{aligned}\right\} \tag{5.2a}$$

$$\left.\begin{aligned} \mathcal{F}=m_2\cos^2(\alpha)+m_3\sin^2(\alpha)=(m_2+m_3\,C^2)/(1+C^2),\\ \mathcal{D}=(m_3-m_2)\sin(\alpha)\cos(\alpha)=(m_3-m_2)\,C/(1+C^2), \end{aligned}\right\} \tag{5.2b}$$

where

$$\alpha=\varphi-\psi, \quad C=\tan\alpha \tag{5.3a,b}$$

($\mathcal{F}(\alpha)$ and $\mathcal{D}(\alpha)$ are the π-periodic functions of the phase lag difference α). The secular systems (4.3) and (5.2) are mathematically equivalent, i.e. getting A, B, ψ, φ from (5.2) computes a, $\bar{a}$, b, $\bar{b}$ and *vice versa*.

The present paper concentrates on the response curves in the $(\bar{\sigma}, A, B)$ space. To exclude the phase lags ψ and φ from (5.2), one can take $\boxed{1}^2+\boxed{3}^2$ and $\boxed{2}^2+\boxed{4}^2$ leading to the two equations with respect to A and B

$$\left.\begin{aligned} A^2[(\Lambda+m_1A^2+\mathcal{F}B^2)^2+(\mathcal{D}B^2+\xi)^2]=\epsilon^2,\\ B^2[(\Lambda+m_1B^2+\mathcal{F}A^2)^2+(\mathcal{D}A^2-\xi)^2]=\delta^2\epsilon^2, \end{aligned}\right\} \tag{5.4}$$

which parametrically depend on α (or $C=\tan\alpha$). An additional equation is needed to compute α. Inserting $\varphi=\psi+\alpha$ into $\boxed{2}$ and $\boxed{4}$ and using expressions for $(\epsilon\cos\psi)$ and $(\epsilon\cos\psi)$ from $\boxed{1}$ and $\boxed{3}$ gives

$$\left.\begin{aligned} (\delta A)[\cos\alpha(\Lambda+m_1A^2+\mathcal{F}B^2)-\sin\alpha(\mathcal{D}B^2+\xi)]-B[\Lambda+m_1B^2+\mathcal{F}A^2]=0,\\ (\delta A)[\cos\alpha(\mathcal{D}B^2+\xi)+\sin\alpha(\Lambda+m_1A^2+\mathcal{F}B^2)]+B[\mathcal{D}A^2-\xi]=0, \end{aligned}\right\} \tag{5.5}$$

which can be treated as a system of linear algebraic homogeneous equations with respect to the amplitude parameters δA and B. When $\delta\neq 0$ (non-longitudinal forcing), the system should have a non-trivial solution ($\delta AB\neq 0$) and, therefore, the zero-determinant condition must be satisfied

$$\begin{aligned} &\sin\alpha\,[\Lambda^2+\xi^2+(m_1+m_3)\Lambda(A^2+B^2)+m_1m_3(A^4+B^4)\\ &\quad+A^2B^2(m_1^2+m_3^2-\cos^2\alpha(m_2-m_3)^2)]+\xi\cos\alpha(m_1-m_2)(B^2-A^2)=0. \end{aligned} \tag{5.6}$$

https://doi.org/10.1017/jfm.2017.263 Published online by Cambridge University Press

The system (5.4), (5.6) governs A^2, B^2 and α for the oblique forcing. When $\delta = 0$ (the longitudinal forcing), (5.5) leads to the equations

$$B[\Lambda + m_1 B^2 + \mathcal{F} A^2] = 0 \quad \text{and} \quad B[\mathcal{D} A^2 - \xi] = 0, \tag{5.7a,b}$$

whose solutions are either $B = 0$ (a planar wave occurring in the excitation plane Oxz) or $B \neq 0$ (three-dimensional sloshing). The planar standing wave is governed by

$$A^2[(\Lambda + m_1 A^2)^2 + \xi^2] = \epsilon^2, \quad B = 0 \tag{5.8a,b}$$

but the three-dimensional sloshing follows from the system

$$\left.\begin{array}{c} A^2[(\Lambda + m_1 A^2 + \mathcal{F}(\alpha) B^2)^2 + (\mathcal{D}(\alpha) B^2 + \xi)^2] = \epsilon^2, \\ \Lambda + m_1 B^2 + \mathcal{F}(\alpha) A^2 = 0, \quad \mathcal{D}(\alpha) A^2 - \xi = 0. \end{array}\right\} \tag{5.9}$$

Remark 1. The steady-state resonant waves by (4.2) always imply either a standing (the two combined Stokes modes in (4.2) are the same) or swirling wave. A criterion for the standing wave is that vectors $(a, \bar{b})$ and $(\bar{a}, b)$ are parallel, i.e.

$$ab = \bar{a}\bar{b} \;\Leftrightarrow\; \sin(\varphi - \psi) = 0, \quad C = \tan(\varphi - \psi) = 0 \;\Leftrightarrow\; \varphi = \psi + \pi i, \quad i = 0, \pm 1, \pm 2, \ldots. \tag{5.10}$$

This means that a standing resonant wave occurs, if and only if, the phase-lag difference is multiple to π ($C = 0$). Otherwise, (4.2) defines swirling.

Remark 2. When $\xi^2 + \delta^2 \neq 0$ (except for the longitudinally excited undamped sloshing), $\cos\alpha \neq 0$. Indeed, if $\delta = 0$ and $\xi \neq 0$ (longitudinally excited damped sloshing), owing to (5.10), the phase-lag difference $\alpha = 0$ for the planar standing waves ($\Rightarrow \cos\alpha = \pm 1$) and the last equation of (5.9), $(m_3 - m_2)\cos\alpha \sin\alpha = \xi \neq 0$ do not allow $\cos\alpha = 0$ for the three-dimensional sloshing. Furthermore, when $\delta \neq 0$ (oblique excitations), assuming $\cos\alpha = 0$ transforms (5.6) to

$$\xi^2 = -(\Lambda + m_1 A^2 + m_3 B^2)(\Lambda + m_1 B^2 + m_3 A^2), \quad \mathcal{F} = m_3 \quad \text{and} \quad \mathcal{D} = 0. \tag{5.11a–c}$$

Inserting ξ^2 into the two equations of (5.4), multiplying these equations and, again, using (5.11) we derive

$$A^2 B^2 \xi^2 (A^2 - B^2)^2 (m_1 - m_3) = \delta^2 \epsilon^4 > 0, \tag{5.12}$$

which is never satisfied for $\delta \neq 0$, since $(m_1 - m_3) < 0$ according to figure 3.

When $\cos\alpha \neq 0$, one can multiply (5.6) by $\cos\alpha$ and rewrite the system (5.4), (5.6) in the form

$$a_2(C^2 + 1) + (a_0 - a_2) + \xi\, a_1 C = 0, \quad b_2(C^2 + 1) + (b_0 - b_2) - \xi\, a_1 C = 0, \tag{5.13a,b}$$

$$C((C^2 + 1)c_3 + c_1) + \xi\, c_0 (1 + C^2) = 0, \tag{5.13c}$$

where

$$\left.\begin{array}{c} a_2 = A^2((\Lambda + m_1 A^2 + m_3 B^2)^2 + \xi^2) - \epsilon^2; \\ b_2 = B^2((\Lambda + m_1 B^2 + m_3 A^2)^2 + \xi^2) - \delta^2 \epsilon^2, \\ a_0 = A^2((\Lambda + m_1 A^2 + m_2 B^2)^2 + \xi^2) - \epsilon^2; \\ b_0 = B^2((\Lambda + m_1 B^2 + m_2 A^2)^2 + \xi^2) - \delta^2 \epsilon^2, \\ a_1 = (m_3 - m_2) A^2 B^2, \\ c_3 = \xi^2 + (\Lambda + m_1 A^2 + m_3 B^2)\,(\Lambda + m_1 B^2 + m_3 A^2), \\ c_1 = -(m_3 - m_2)^2 A^2 B^2, \quad c_0 = (m_1 - m_2)(B^2 - A^2). \end{array}\right\} \tag{5.14}$$

https://doi.org/10.1017/jfm.2017.263 Published online by Cambridge University Press

Remark 3. The coefficients at C and C^2 in (5.13*a*,*b*) have equal asymptotic order, namely, $b_2 \sim b_0 \sim a_2 \sim a_0 \sim \xi\, a_1 = O(\epsilon^2)$. It can happen that solving the system (5.13) gives a small non-zero C, i.e.

$$0 \neq |C| \lesssim O(\epsilon^{1/3}) = O(\sqrt{A^2 + B^2}). \tag{5.15}$$

Formally, this solution implies a swirling wave mode (Remark 1 above). However, by treating (5.13*a*,*b*) in an asymptotic sense on the $\epsilon^{1/3}$ scale and neglecting the $O(\epsilon^2)$ terms leads to $b_0 = a_0 = 0$, which are equations for a standing wave regime. This formal mathematical conflict can be resolved by interpreting (5.15) as a condition for an almost standing wave mode. Ikeda *et al.* (2012, figure 4*g*) experimentally observed those modes.

5.2. *Undamped steady-state resonant sloshing for oblique excitations*

When $0 < \delta \leqslant 1$ ($0 < \gamma \leqslant \pi/4$), the steady-state analysis can be done by using (5.13) with $\xi = 0$, which takes the form

$$a_2^0(C^2+1) + (a_0^0 - a_2^0) = 0, \quad b_2^0(C^2+1) + (b_0^0 - b_2^0) = 0, \quad C(c_3^0(C^2+1) + c_1) = 0, \tag{5.16a–c}$$

where

$$\left.\begin{array}{c} a_2^0 = A^2(\Lambda + m_1A^2 + m_3B^2)^2 - \epsilon^2; \quad b_2^0 = B^2(\Lambda + m_1B^2 + m_3A^2)^2 - \delta^2\epsilon^2, \\ a_0^0 = A^2(\Lambda + m_1A^2 + m_2B^2)^2 - \epsilon^2; \quad b_0^0 = B^2(\Lambda + m_1B^2 + m_2A^2)^2 - \delta^2\epsilon^2, \\ c_3^0 = (\Lambda + m_1A^2 + m_3B^2)\,(\Lambda + m_1B^2 + m_3A^2). \end{array}\right\} \tag{5.17}$$

The third equation of (5.16) yields the alternative: either $C = 0$ or $c_3(C^2+1) + c_1 = 0$. Because of the standing wave criterion (5.10), the first case implies a standing wave, but the second case corresponds to swirling.

Inserting $C = 0$ into (5.16) reduces them to the equality $a_0^0 = b_0^0 = 0$, which has the analytical solution

$$B^2((m_1 - m_2)(B^2 - A^2) \pm \epsilon/A)^2 = \delta^2\epsilon^2, \quad \Lambda = \pm\epsilon/A - m_1A^2 - m_2B^2. \tag{5.18a,b}$$

The analytical solution suggests solving the first (cubic) equation (from one to three positive roots $B^2 > 0$) for a given $\pm A$ and, thereafter, computing Λ for these $\pm A$ and B (the second equation).

When $C \neq 0$, substituting $(C^2+1) = -c_1/c_3 > 1$ into the two first equations of (5.16) derives the system

$$\left.\begin{array}{c} (\Lambda + m_1A^2 + m_3B^2)D(\Lambda; A, B) = (m_2 - m_3)\epsilon^2, \\ (\Lambda + m_1B^2 + m_3A^2)D(\Lambda; A, B) = (m_2 - m_3)\delta^2\epsilon^2, \\ 0 < (\Lambda + m_1A^2 + m_3B^2)(\Lambda + m_1B^2 + m_3A^2) \leqslant (m_3 - m_2)^2A^2B^2, \end{array}\right\} \tag{5.19}$$

where the function

$$\begin{aligned} D(\Lambda; A^2, B^2) \;=\; & 2\Lambda^2 + \Lambda(A^2 + B^2)(2m_1 + m_2 + m_3) \\ & + m_1(m_2 + m_3)(A^4 + B^4) + 2(m_1^2 + m_2m_3)A^2B^2 \end{aligned} \tag{5.20}$$

commutates by variables A^2 and B^2. The structure of (5.19) requires

$$\Lambda(1 - \delta^2) + (m_3 - \delta^2m_1)A^2 + (m_1 - \delta^2m_3)B^2 = 0, \tag{5.21}$$

which, because $(m_3 - \delta^2m_1) > 0$ for $0.5 \lesssim h/L$ (figure 3), makes it possible to express A^2 as a linear combination of B^2 and Λ. Substituting this expression into

https://doi.org/10.1017/jfm.2017.263 Published online by Cambridge University Press

the first/second equation of (5.19) derives a cubic equation with respect to B^2 whose coefficients are functions of Λ. This means that, for any fixed Λ, we can find the real positive roots B^2 as functions of Λ, but (5.21) returns the corresponding A^2. One can say that we have an analytical solution for $C \neq 0$.

The undamped steady-state resonant sloshing due to an oblique harmonic excitation with $0 < \delta < 1$ $(0 < \gamma < \pi/4)$ can theoretically lead to a maximum six different standing steady-state resonant waves (three for A and three for $-A$, by (5.18)). Each point on the corresponding response curves in the $(\sigma/\sigma_1, A, B)$ space determines a single steady-state wave from these six solutions. In contrast, Part 1 reports three standing waves for longitudinal and diagonal harmonic excitations, which consist of one planar and two square-like resonant waves so that any point on the square-like response curves corresponds to two physically identical Stokes waves occurring with an angle to the excitation plane.

Equations (5.19) and $(C^2 + 1) = -c_1/c_3 \geqslant 1$ determine a maximum three physically different undamped swirling waves. Each point on the corresponding curves implies two physically identical swirling waves (clockwise and counterclockwise) associated with (Λ, A, B, C) and $(\Lambda, A, B, -C)$. By analysing $\boxed{3}$ $(AB^2\mathcal{D}(\alpha) = \epsilon \sin\psi)$ and $\boxed{4}$ $(A^2B\mathcal{D}(\alpha) = \delta\epsilon \sin\varphi)$, we derive these two waves as $z = S(x, y; A\cos\psi, B\cos\varphi)\cos\bar{\sigma}t + S(x, y; A\sin|\psi|, B\sin|\varphi|)\sin\bar{\sigma}t + O(\epsilon^{1/3})$ and $z = S(x, y; A\cos\psi, B\cos\varphi)\cos\bar{\sigma}t - S(x, y; A\sin|\psi|, B\sin|\varphi|)\sin\bar{\sigma}t + O(\epsilon^{1/3})$. The results for the undamped swirling are consistent with Part 1 where only longitudinal and diagonal harmonic excitations were considered.

5.3. *Damped steady-state resonant sloshing*

Except for the longitudinal forcing, we do not know how to construct an analytical solution of the secular equations for the damped sloshing with $O(\epsilon^{2/3}) = \xi > 0$. However, one can classify the corresponding steady-state solutions by using the standing wave criterion (5.10). When $A, B \geqslant 0$ and $\xi > 0$ in equations $\boxed{3}$ and $\boxed{4}$, the criterion leads to

$$\psi = \varphi + 2\pi i, \quad i \in \mathbb{Z} \quad \text{and} \quad B = \delta A. \tag{5.22}$$

5.3.1. *Longitudinal forcing*

When $\delta = 0$ and $\xi > 0$, (5.8) transforms (5.2*a*) to the form (5.7), which we rewrite as

$$\left.\begin{gathered} A^2(\xi^2 + [\Lambda + m_1A^2]^2) = \epsilon^2, \\ 0 < A \leqslant \epsilon/\xi; \quad B = 0; \quad 0 \leqslant \psi = \varphi = \arccos A\,[\Lambda + m_1A^2]/\epsilon \leqslant \pi. \end{gathered}\right\} \tag{5.23}$$

The roots describe the planar steady-state standing wave for the first Stokes mode

$$z = A\cos(\bar{\sigma}t - \psi) f_1^{(1)}(x) + O(\epsilon^{1/3}). \tag{5.24}$$

The square-like standing waves are impossible for the damped sloshing.

To describe swirling, we rewrite (5.9) in the form

$$\left.\begin{gathered} A\left[\Lambda + m_1A^2 + \frac{m_2 + m_3C^2}{1 + C^2}B^2\right] = \epsilon\cos\psi; \quad A\left[\frac{(m_3 - m_2)C}{1 + C^2}B^2 + \xi\right] = \epsilon\sin\psi; \\ B^2 = -\frac{1}{m_1}\left[\Lambda + \frac{m_2 + m_3C^2}{1 + C^2}A^2\right] > 0; \quad A^2 = \frac{\xi(1 + C^2)}{(m_3 - m_2)C} > 0. \end{gathered}\right\} \tag{5.25}$$

https://doi.org/10.1017/jfm.2017.263 Published online by Cambridge University Press

Consequently substituting expressions for A^2 and B^2 into the square sum of the first row equations gives a nonlinear algebraic equation with respect to C:

$$q_6C^6+q_5C^5+q_4C^4+q_3C^3+q_2C^2+q_1C+q_0=0, \tag{5.26}$$

where

$$\left.\begin{aligned} q_6&=\xi^3(m_1^2-m_3^2)^2>0,\\ q_5&=2\xi^2\Lambda(m_3-m_2)(m_3+m_1)(m_1-m_3)^2,\\ q_4&=\xi\,[\xi^2[3m_1^4+(m_2^2-6m_2m_3-m_3^2)m_1^2-2m_1m_3(m_2-m_3)^2+m_2m_3^2(m_2+2m_3)]\\ &\quad+\Lambda^2(m_2-m_3)^2(m_1-m_3)^2],\\ q_3&=\epsilon^2(m_2-m_3)^3m_1^2+2\Lambda\xi^2\,[m_1(m_2^3-m_2^2m_3+m_2m_3^2-m_3^3)\\ &\quad+(m_2-m_3)(m_1^2(m_2+m_3-2m_1)-m_2m_3(m_2+m_3))],\\ q_2&=\xi\,[\Lambda^2(m_2-m_3)^2(m_1-m_2)^2\\ &\quad+\xi^2[3m_1^4+(-m_2^2-6m_2m_3+m_3^2)m_1^2-2m_1m_2(m_2-m_3)^2+m_2^2m_3(2m_2+m_3)]],\\ q_1&=2\xi^2\Lambda\,(m_3-m_2)(m_1+m_2)(m_1-m_2)^2,\\ q_0&=\xi^3(m_1^2-m_2^2)^2>0 \end{aligned}\right\} \tag{5.27}$$

are functions of Λ. The polynomial equation (5.26) has maximum six positive roots C ($(m_3-m_2)>0$ in the last formula of (5.25)). Substituting these roots into expressions for A^2 and B^2 of (5.25) computes $(\sigma/\sigma_1,\ A,\ B,\ C)$, which implies a point on the corresponding response curves. Because $\delta=0$, a unique phase lag φ cannot be found; φ are restored for each $C=\tan\alpha$ as $\varphi_1=\psi+\alpha$ and $\varphi_2=\psi+\alpha\pm\pi$. Physically, these two phase lags $\varphi_{1,2}$ for each point $(\sigma/\sigma_1, A, B, C)$ on the response curves mean that the point determines two physically identical swirling waves (clockwise and counterclockwise).

5.3.2. *Diagonal forcing*

When $\delta=1$, (5.22) transforms (5.2*a*) to the form

$$\left.\begin{aligned} &A^2(\xi^2+[\Lambda+(m_1+m_2)A^2]^2)=\epsilon^2,\\ A=B>0,\quad &0\leqslant\psi=\varphi=\arccos A\,[\Lambda+(m_1+m_2)A^2]/\epsilon\leqslant\pi, \end{aligned}\right\} \tag{5.28}$$

whose solution describes the diagonal wave

$$z=A\cos(\bar\sigma t-\psi)\,S(x,y;1,1)+O(\epsilon^{1/3}) \tag{5.29}$$

by the combined diagonal-type Stokes mode $S(x, y; 1, 1)$. The square-like standing waves are impossible for the diagonally forced damped sloshing.

Diagonally forced undamped sloshing requires $A=B$ (the wave amplitudes are equal in the Ox and Oy directions). This fact was extensively discussed in Part 1. Substituting $A=B$ into $\boxed{1}$ and $\boxed{2}$ of (5.2*a*) for the damped sloshing ($\xi>0$) leads to either $\varphi=\psi$ (corresponding to the diagonal wave) or $\varphi=-\psi$. The latter condition means that the left-hand sides of $\boxed{3}$ and $\boxed{4}$ are equal and, therefore, $2A\xi=2B\xi=(A+B)\xi=0$, which is impossible. As a consequence, the diagonally forced swirling is characterised by non-equal wave responses along the perpendicular walls.

5.3.3. *Oblique forcing*

When $0<\delta<1$, substituting the standing wave criterion (5.22) into (5.2) and taking the difference of $\boxed{1}$ and $\boxed{2}$ we derive $(m_1-m_2)(1-\delta^2)A^3=0$. Figure 3 shows that

https://doi.org/10.1017/jfm.2017.263 Published online by Cambridge University Press

$m_1 > m_2$ and, therefore, this equality is never fulfilled. As a consequence, the standing resonant wave regime is not possible for oblique non-diagonal forcing with $0 < \delta < 1$. All steady-state resonant waves are formally of the swirling type.

5.3.4. *Summary*

Theoretical results on the damped resonant sloshing in §§ 5.3.1–5.3.3 show that (a) the standing resonant waves exist only for longitudinal and diagonal harmonic excitations, these are of planar or diagonal type, respectively, (b) the square-like standing waves are impossible, (c) for the oblique non-diagonal forcing with $0 < \delta < 1$, all the damped steady-state sloshing regimes are of the swirling type, (d) when the asymptotic condition (5.15) (the non-zero C is relatively small) is satisfied, the corresponding swirling becomes close to a standing wave of a modified Stokes mode so that it can be treated as an almost standing wave, (e) two physically identical swirling waves of the opposite angular directions are only possible for the longitudinal forcing, (f) for the oblique forcing with $\gamma \neq 0$, each point on the response curves implies a unique swirling wave whose amplitudes along the Ox and Oy axes are never equal, even for the diagonal forcing.

6. Damped versus undamped response curves

The undamped response curves for the longitudinal forcing ($\delta = \gamma = 0$) were extensively analysed and discussed in Part 1 for various liquid depths and forcing amplitudes. Figure 4(*a*) shows the corresponding response curves in terms of the 'integral' amplitudes A and B, which present the dominant sin and cos components in a_1 and b_1. To get A and B, we use, in fact, an exact asymptotic solution of the modal system constructed in appendix A. The solution neglects the $O(\epsilon)$-quantities but the modal equations (2.6)–(2.7) are also derived within to the $O(\epsilon)$-order sloshing component.

In our numerical analysis, we will present a three-dimensional view in the $(\sigma/\sigma_1, A, B)$ space and its projections onto the $(\sigma/\sigma_1, A)$ and $(\sigma/\sigma_1, B)$ planes. Panel (*b*) of the figure depicts the corresponding response curves for the damped sloshing ($\xi = 0.0256$). The solid lines specify stable solutions. The computations were done with the non-dimensional forcing amplitude $\eta = \eta_{1a} = 0.0075\,(\eta_{2a} = 0)$ and $h/L = 0.6$. Because m_1, m_2 and m_3 weakly depend on h/L for $0.5 \lesssim h/L$, the branching should be similar for these relatively high liquid depth-to-tank breadth ratios. The latter fact is also true for figures 5–8 where we present the response curves for the oblique forcing with $\gamma = \pi/36 = 5^\circ$, $\pi/6 = 30^\circ$, $\pi/4.5 = 40^\circ$ and $\pi/4 = 45^\circ$, respectively. Henceforth, the small letters (p_0, d_0, s_0 and d_1) are used to specify the fact that the corresponding branches meet at the infinity.

The undamped planar sloshing corresponds to $B = 0$, $C = 0$, $\xi = 0$ and $A > 0$ in (5.8) so that the non-zero amplitude A is then governed by the cubic equation $A(\Lambda + m_1 A^2) = \epsilon$ (see, condition (5.10) and equations (5.4), (5.7) with $\delta = \xi = 0$). The phase lags are $\psi = 0$ for $(\Lambda + m_1 A^2) > 0$ and $\psi = \pi$ as $(\Lambda + m_1 A^2) < 0$. The second phase lag φ is associated with the zero cross-wave component ($B = 0$) and therefore it has no a physical meaning. Because the standing wave condition (5.10) requires $\sin(\varphi - \psi) = 0$, one can take $\varphi = \psi$. The undamped planar steady-state waves are represented by the branches $P_l TEp_0$ and $P_r Wp_0$ in figure 4(*a*). The branches belong to the $(\sigma/\sigma_1, A)$ plane. They are invisible (coincide with the horizontal axis) in projection onto the $(\sigma/\sigma_1, B)$ plane. An extensive discussion of the turning point T and the bifurcation points E and W can be found in Part 1. The bifurcation points E and W are origins of the square-like and swirling waves, respectively. The planar resonant waves are stable for the forcing frequencies to the left of T and to the right of W.

https://doi.org/10.1017/jfm.2017.263 Published online by Cambridge University Press

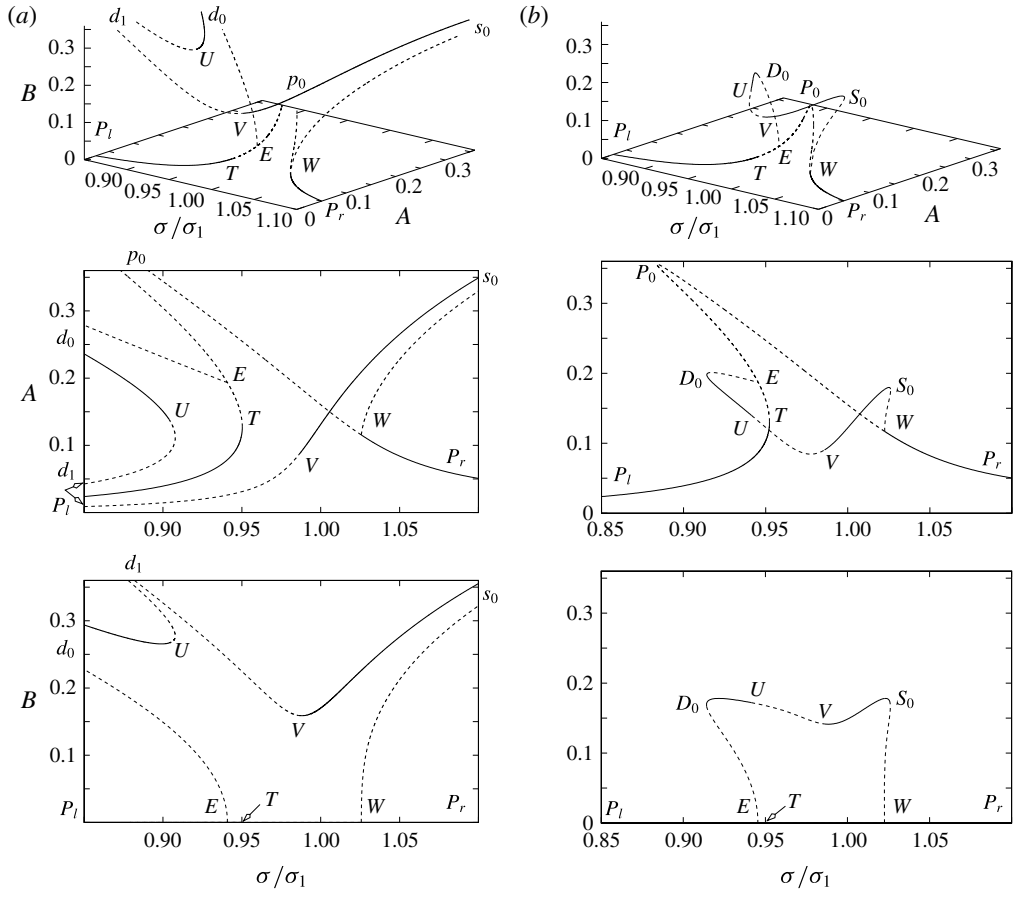


FIGURE 4. The steady-state wave response curves in the $(\sigma/\sigma_1, A, B)$ space and their projection onto the $(\sigma/\sigma_1, A)$ and $(\sigma/\sigma_1, B)$ planes for the undamped (a) and damped (b) cases. The longitudinal forcing with the non-dimensional amplitude $\eta = \eta_{1a} = 0.0075$ and $h/L = 0.6$. The solid lines specify stable solutions. The branches $P_lTEP_0(p_0)$ and $P_rWP_0(p_0)$ belong to the $(\sigma/\sigma_1, A)$ plane. They correspond to the planar standing waves. The small letters p_0, d_0, d_1 and s_0 in (a) mean that the corresponding branches meet at the infinity. The square-like standing waves exist for the undamped case (a). They are presented by the two branches d_1Ud_0 and d_0E. The undamped swirling corresponds to Ws_0Vd_1. The square-like waves disappear in the damped case (b). The branch ED_0UVS_0W represents in (b) a swirling wave mode. However, computations show that condition (5.15) is satisfied on the stable sloshing subbranch D_0U and, therefore, the subbranch represents an almost standing wave by a modified Stokes mode (close to a square-like wave in (a)). All steady-state waves are unstable in the frequency range between T and V where irregular (chaotic) wave motions are expected. Results in (a) are based on computation schemes from Part 1. Computational formulas for getting (b) are presented in § 5.3.1.

Setting $\xi = 0$ in (5.9) makes it possible to consider the three-dimensional undamped steady-state sloshing with $B \neq 0$ due to the longitudinal forcing. The last equation of (5.9) deduces that $\mathcal{D}(\alpha) = 0$ and, thereby, we arrive at the alternative: either $\sin\alpha = 0$ or $\cos\alpha = 0$. Because of (5.10), the first case ($\sin\alpha = 0$) implies three-dimensional

https://doi.org/10.1017/jfm.2017.263 Published online by Cambridge University Press

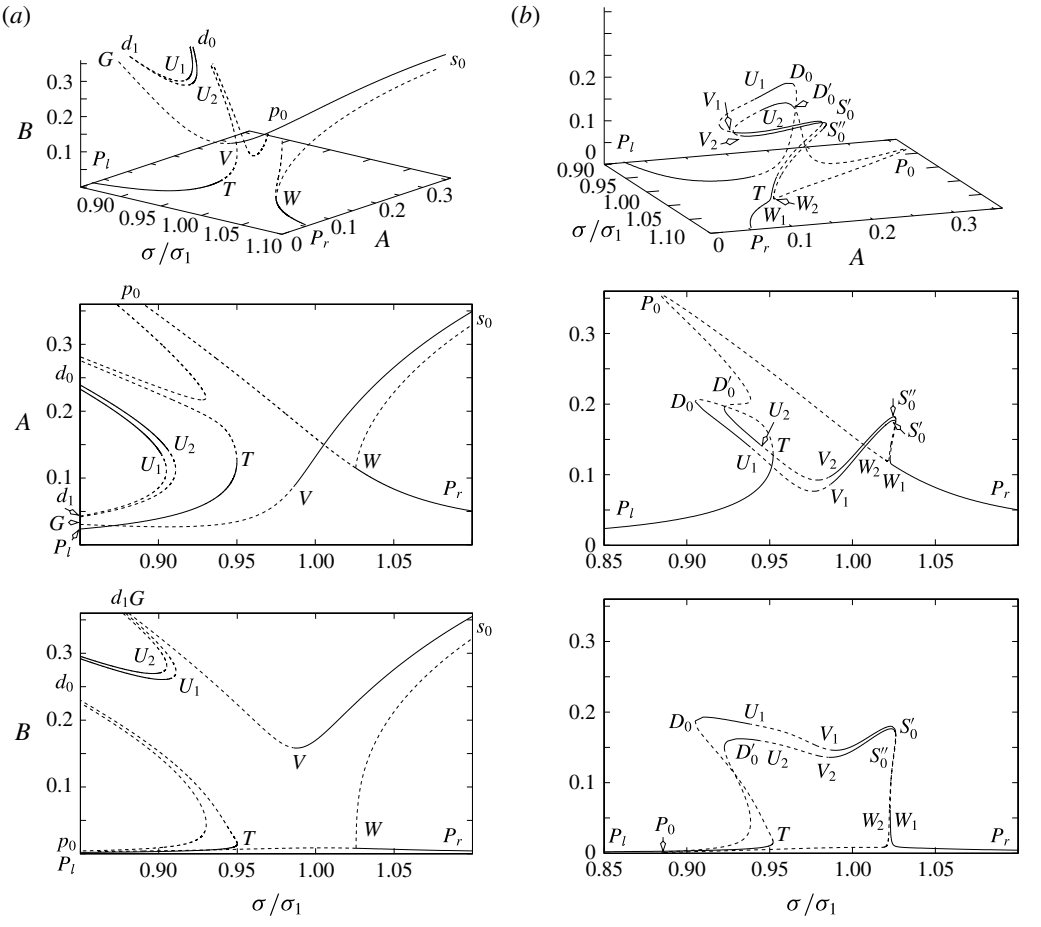


FIGURE 5. Similar to figure 4 but for an oblique forcing with $\gamma = 5^\circ = \pi/36$. The non-zero γ splits the connected branch $P_lT(E)p_0(P_0)$ in figure 4 at the bifurcation point E. The undamped case (a) is characterised by five categories of standing resonant waves (a maximum of six are possible according to the theory). They are represented by the branches P_lTd_0, d_0p_0, $d_1U_1d_0$, $d_1U_2d_0$ and P_rWp_0. Each point on these branches implies a single standing wave type (not two as in figure 4 for the square-like wave mode). Because γ is relatively small, the stable subbranches P_lT and P_rW correspond to the nearly planar standing waves. The swirling-related branches are Ws_0 and s_0VG where G belongs to $d_1U_1d_0$ (and has coordinates $(\sigma/\sigma_1, A, B) = (0.83, 0.04, 0.4)$ in this numerical example). In (b), the non-zero damping and angle γ split the response curves at both E and W from figure 4. There appear two non-connected branches $P_lTD_0U_1V_1S_0'W_1P_r$ and (loop-like) $P_0D_0'U_2V_2S_0''W_2P_0$. Formally, each of the points on these branches imply a single (stable/unstable) swirling wave. Computations show that (5.15) is satisfied on the stable subbranches P_lT and P_rW_1 (almost planar wave) as well as on U_1D_0 and U_2D_0'. The point G in (a) coincides with U_1 for the damped case (b). Results in (a) are based on (5.18) (standing waves) and (5.19) (swirling). Results for (b) are a numerical solution of (5.13) (computational details are given in supplementary materials available at https://doi.org/10.1017/jfm.2017.263).

https://doi.org/10.1017/jfm.2017.263 Published online by Cambridge University Press

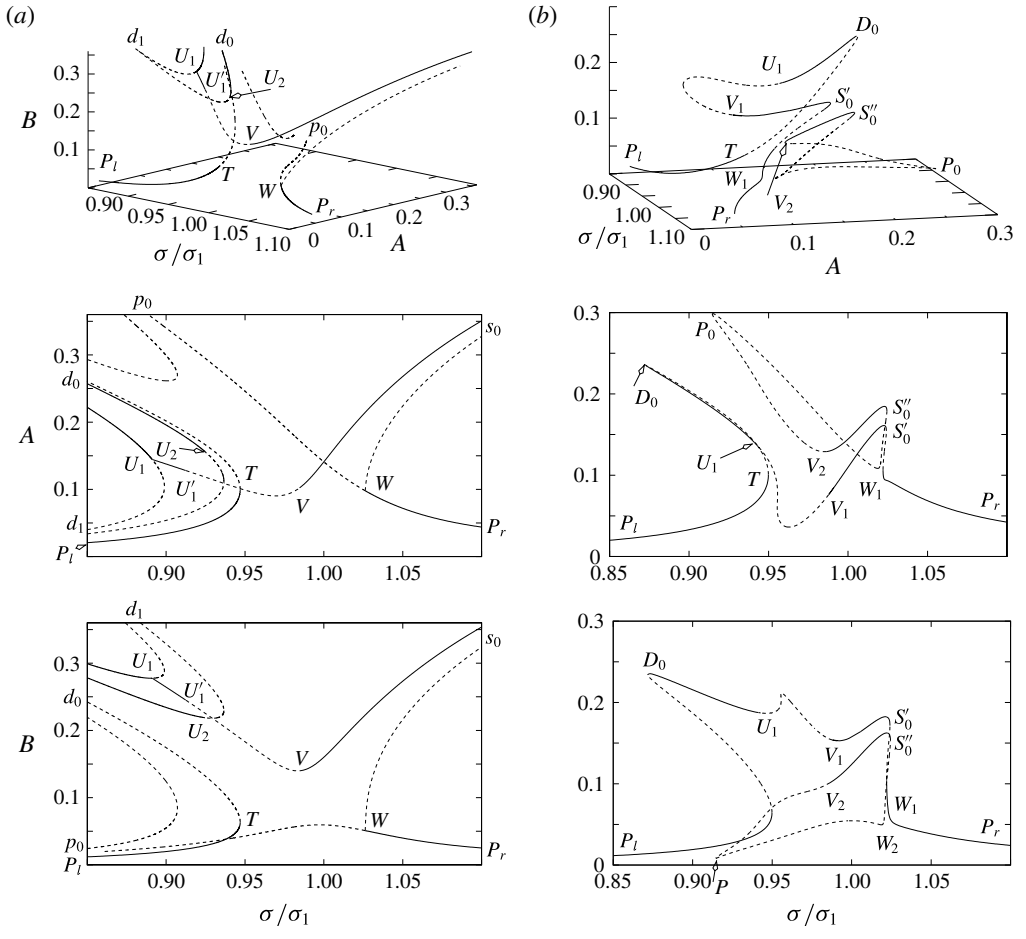


FIGURE 6. The same as in figure 5 but for $\gamma = 30^\circ$. A novelty in (a) (undamped sloshing) is that an extra stable swirling subbranch U_1U_1' appears with increasing γ. The damped sloshing response curves in (b) show the vanishing of the stable almost standing waves (U_1D_0' in figure 5b). The loop-like branch $P_0S_0''V_2P_0$ has now only one stable piece V_2S_0'' corresponding to swirling (condition (5.15) is not satisfied). Results in (a) are based on (5.18) (standing waves) and (5.19) (swirling). Results for (b) are a numerical solution of (5.13) (computational details are given in supplementary materials).

(non-planar) standing waves, which are, as we know from Part 1, the square-like resonant steady-state sloshing. When $\cos\alpha = \cos(\varphi - \psi) = 0$, the secular equations (5.9) with $\xi = 0$ govern the undamped swirling.

Substituting $\sin\alpha = 0$ in (5.9) derives $A^2(\Lambda + m_1A^2 + m_2B^2)^2 = \epsilon^2$ and $(\Lambda + m_1B^2 + m_2A^2) = 0$, which govern the non-dimensional amplitudes A and B of the square-like wave regime. The phase lag $\psi = 0$ for $(\Lambda + m_1A^2 + m_2B^2) > 0$ and $\psi = \pi$ when $(\Lambda + m_1A^2 + m_2B^2) < 0$. Another phase lag φ follows from the standing wave condition (5.10), $\sin(\varphi - \psi) = 0$. It equals to either $\varphi = \psi$ or $= \psi \pm \pi$. The non-uniqueness of φ implies two different square-like waves for each point of the corresponding response curves in the $(\sigma/\sigma_1, A, B)$ space. These two square-like standing waves are defined by $z = \pm S(x, y; A, B)\cos\bar{\sigma}t + O(\epsilon^{1/3})$ and $z = \pm S(x, y; A, -B)\cos\bar{\sigma}t + O(\epsilon^{1/3})$.

https://doi.org/10.1017/jfm.2017.263 Published online by Cambridge University Press

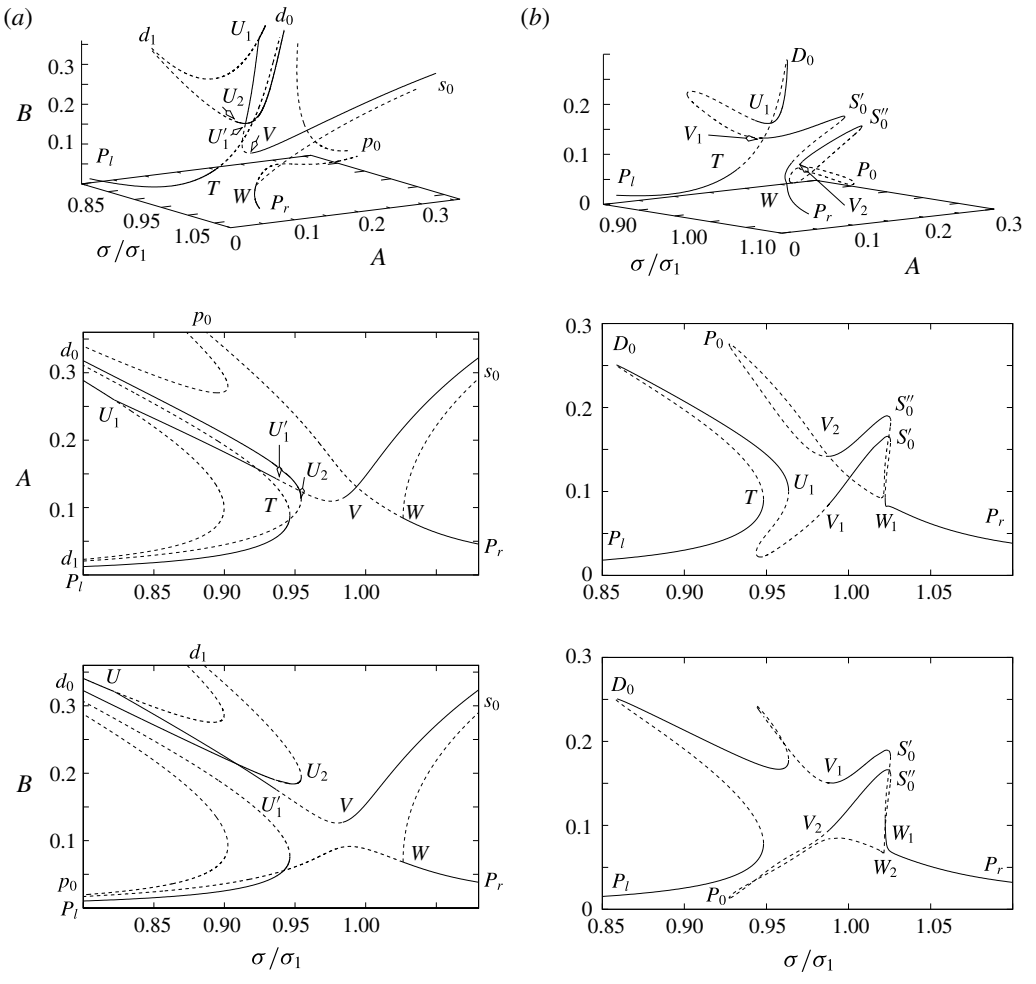


FIGURE 7. The same as in figure 6 but for $\gamma = 40°$. For the undamped case in (a), the subbranches $d_0U_1U_1'Vs_0$, Ws_0 and U_2d_0 tend to the $A = B$ plane. The first two subbranches convert to the undamped swirling but U_2d_0 should turn into the diagonal standing wave (the limit is shown in figure 8a). In (b), the swirling-related response curves do not belong to the $A = B$ plane as $\gamma \to \pi/4$. As a consequence, only U_1D_0 tends to the plane. It converts to the diagonal standing wave for $\gamma = \pi/4$. Results in (a) are based on (5.18) (standing waves) and (5.19) (swirling). Results for (b) are a numerical solution of (5.13) (computational details are given in supplementary materials).

They can be treated as occurring with an equal (positive and negative) angle relative to the forcing plane Oxz. The square-like sloshing is presented in figure 4(a) by the two branches Ed_0 and d_1Ud_0. The (unstable waves) branch Ed_0 emerges from the bifurcation point E. Point U divides d_1Ud_0 into Ud_0 (stable square-like sloshing) and Ud_1 (unstable one).

In the second case ($\cos\alpha = \cos(\varphi - \psi) = 0$, undamped swirling), amplitudes A and B are computed from $A^2(\Lambda + m_1A^2 + m_3B^2)^2 = \epsilon^2$ and $(\Lambda + m_1B^2 + m_3A^2) = 0$. The first phase lag $\psi = 0$ for $(\Lambda + m_1A^2 + m_3B^2) > 0$ and $\psi = \pi$ when $(\Lambda + m_1A^2 + m_3B^2) < 0$. Because $\delta = 0$, the second phase lag φ cannot be directly computed by

https://doi.org/10.1017/jfm.2017.263 Published online by Cambridge University Press

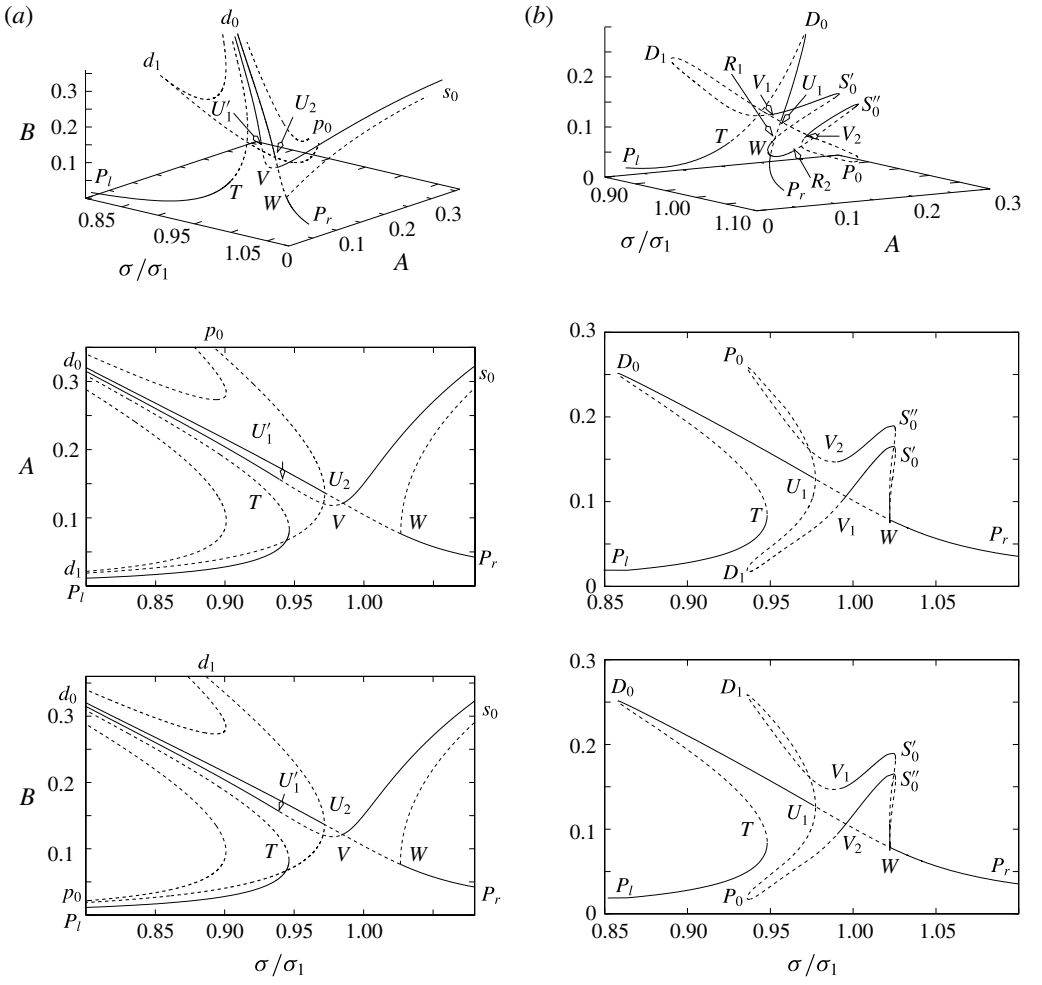


FIGURE 8. The same as in figure 6 but for the diagonal forcing with $\gamma = 45^\circ = \pi/4$. In ($a$), all branches away from the $A = B$ plane correspond to the square-like standing wave regime; U_2 is the corresponding bifurcation point for this regime. The branches P_lTd_0, P_rW and U_2d_0 imply diagonal standing waves. The branches $d_0U_1'Vs_0$ and Ws_0 correspond to swirling (two physically identical waves in the clockwise and counterclockwise directions, respectively). Only diagonal standing waves belong to the $A = B$ plane in the damped case (b) the branch $P_lTD_0WP_r$. The (stable sloshing) subbranches WR_1, WR_2, $S_0'V_1$ and $S_0''V_2$ correspond to swirling (condition (5.15) is not satisfied on them). Results in (a) are based on (5.18) (standing waves) and (5.19) (swirling). Results for (b) are a numerical solution of (5.13) (computational details are given in supplementary materials).

using (5.2a). Requiring $\cos\alpha = 0$ deduces however that $\varphi = \psi \pm \pi/2$. Accounting for (4.2) and (5.1c–f), $\pm\pi/2$ for φ implies two swirling waves for each point on the corresponding branches in the $(\sigma/\sigma_1, A, B)$ space. These two waves are $z = \pm(Af_1^{(1)}(x)\cos\bar{\sigma}t + Bf_1^{(2)}(y)\sin\bar{\sigma}t) + O(\epsilon^{1/3})$ and $z = \pm(Af_1^{(1)}(x)\cos\bar{\sigma}t - Bf_1^{(2)}(y)\sin\bar{\sigma}t) + O(\epsilon^{1/3})$. They are physically identical and only differ by the propagating angle direction, clockwise or counterclockwise. The undamped swirling

https://doi.org/10.1017/jfm.2017.263 Published online by Cambridge University Press

regime is represented by the branches Ws_0 and d_1Vs_0 in figure 4(*a*). The (unstable swirling) branch Ws_0 emerges from the planar-wave response curves at the bifurcation point W. Another swirling-related branch d_1Vs_0 is divided by V into stable and unstable subbranches.

For the undamped longitudinally forced sloshing, irregular (chaotic) waves are possible for the forcing frequencies laying between the abscissas of T and V. This fact was extensively discussed in Part 1.

The response curves for the damped steady-state sloshing due to the longitudinal forcing are drawn by using the analytical solution (5.23)–(5.26). Figure 4(*b*) illustrates the numerical output for $\xi = 0.0256$. According to our results from § 5.3.1, the damped square-like waves are impossible. The connected branch $P_lTEP_0WP_r$ belongs to the $(\sigma/\sigma_1, A)$-plane; it is responsible for the planar waves (P_0 is not at the infinity). The damping saves the two bifurcation points E and W. These points are now two origins for the damped swirling, which is represented by the arc-like branch ED_0UVS_0W. The points D_0 and S_0 are not at infinity now; d_1 disappears. Computations show that the asymptotic condition (5.15) is satisfied on the (stable sloshing) subbranch D_0U. This means that the subbranch represents an almost standing wave when a modified Stokes mode dominates. This mode is close to a square-like wave on Ud_0 in (*a*). The linear damping ratio $\xi = 0.0256$ gives a negligible effect on positions of V and T. As a consequence, the frequency range, where irregular waves are expected, remain almost the same in (*a*,*b*).

One should note that Ikeda *et al.* (2012) detected, numerically and experimentally, both irregular and regular (periodic) damped sloshing in the frequency range between T and V. They used an adaptive multimodal system with linear damping terms for simulations. Dedicated model tests are needed to quantify whether the regular sloshing exists and, thereby, clarify whether one should switch to an adaptive asymptotic ordering from the Narimanov–Moiseev one for a more accurate description of the resonant sloshing in this frequency range.

Almost longitudinal forcing ($\gamma = \pi/36 = 5^\circ$) is considered in figure 5. When comparing the undamped sloshing in (*a*) of figures 4 and 5, one should remember that the oblique forcing admits up to six different standing waves. We identify five categories of those standing waves represented by the branches P_lTd_0, d_0p_0, d_1U1d_0, $d_1U_2d_0$ and P_rWp_0. The former d_1Ud_0 in figure 4(*a*) splits into the two branches $d_1U_1d_0$ and $d_1U_2d_0$, but the bifurcation point E vanishes so that the former P_lTEp_0 is divided into P_lTd_0 and d_0p_0. In contrast to the longitudinal forcing in figure 4(*a*), each point on the branches implies only one unique standing wave. Two pieces of P_rWp_0 and P_lTd_0 are close to the horizontal plane $B = 0$; they imply an almost planar stable steady-state wave regime. Other points on the aforementioned five branches correspond to a square-like standing wave. The swirling wave regime is represented by Ws_0 and s_0VG. A novelty is that the latter branch meets $d_1U_1d_0$ at a point G (coordinates $(\sigma/\sigma_1, A, B) = (0.83, 0.04, 0.4)$ in this numerical example). Each point on the swirling-related branches corresponds to two identical (clockwise and counterclockwise) swirling waves.

A complex effect of the non-zero γ and damping on the response curves is demonstrated in figure 5(*b*). The branching should be compared with that in figure 4(*b*) as well as with (*a*). We see that $\xi = O(\epsilon^{2/3})$ and a relatively small γ split the response curves at both E and W from figure 4. As a consequence, the two non-connected branches $P_lTD_0U_1V_1S_0'W_1P_r$ and (loop-like) $P_0D_0'U_2V_2S_0''W_2P_0$ appear. Both of them have very attractive geometry, especially, in the $(\sigma/\sigma_1, A, B)$ space. Each point on these response curves implies swirling. However, computations show that (5.15) is

https://doi.org/10.1017/jfm.2017.263 Published online by Cambridge University Press

satisfied on the stable subbranches P_lT and P_rW_1 (almost planar wave) as well as on U_1D_0 and U_2D_0'. The point G from (a) coincides with U_1 for the damped case. The most important effect of the non-zero γ for an oblique forcing is that the two physically identical swirling waves (clockwise and counterclockwise) split into two different ones. We can see this effect by comparing (a) and (b) in figure 5. Condition (5.15) is satisfied on V_1S_0' and V_2S_0'' and, therefore, two swirling waves of different amplitudes along the Ox and Oy axes are expected represented by these stable sloshing subbranches.

Figures 6 and 7 demonstrate what happens with the response curves with a further increase of γ. The trends are different for the damped and undamped cases. The (a) show that, after G met U_1, an extra subbranch U_1U_1' appears, which implies a stable swirling. With increasing γ close to $\pi/4$, U_1 moves away from the primary resonance zone, but $U_1U_1'Vs_0$ tends to lie in the $A=B$ plane. The latter will be responsible for the diagonally excited swirling in figure 8. Another subbranch U_2d_0 also approaches the $A=B$ plane; it corresponds to the diagonal wave as $\gamma=\pi/4$. The damped sloshing response curves in (b) of figures 6 and 7 show that the linear damping erases the U_2D_0' subbranch for non-small γ. They also confirm that the plane $A=B$ contains only response curves of the diagonal wave regime.

The diagonal wave regime for $\gamma=\pi/4$ (diagonal forcing) is characterised by three stable sloshing subbranches. They must belong to the $A=B$ plane. Figure 8 shows the latter fact for both damped and undamped sloshing. The subbranches P_lT and P_rW transform from the stable planar waves as γ changes from 0 to $\pi/4$. Part 1 describes another stable diagonal sloshing subbranch, which should be situated over P_lT. The limit $\gamma\to\pi/4$ shows that the third subbranch results from the stable standing wave regimes on U_2d_0 but because the linear damping annihilates U_2D_0', the stable diagonal waves are represented by U_1D_0.

7. Comparison with experiments

Ikeda *et al.* (2012) conducted relevant experimental studies on the steady-state wave regimes for the damped liquid sloshing. The maximum wave elevations near the two perpendicular walls (at the points $(x_0L,0)$ and $(0,x_0L)$ with $x_0=0.4$) were measured including for standing, swirling and irregular wave motions. The experimental data are reported for the longitudinal ($\gamma=0$), oblique ($\gamma=\pi/6$) and diagonal ($\gamma=\pi/4$) cases. The forcing amplitudes are slightly different and equal to $\eta=0.00727$, 0.00726 and 0.00717, respectively. In the model tests, the liquid depth ratio is $h/L=0.6$. Before presenting the experimental measurements, they extensively discussed in their figure 4, what kind of stable and unstable steady-state resonant waves are observed for these three experimental cases. This includes a discussion on the stable waves, which normally correspond to the standing (planar and diagonal) waves, or what we called an almost standing waves (see, discussion around the asymptotic condition (5.15)). A special emphasis of Ikeda *et al.* (2012) was also placed on the fact that two swirling waves with different angular directions are characterised by different maximum elevations at the measurement probes for the non-longitudinal forcing.

These experimental measurements of the L-scaled maximum steady-state wave elevations, ζ_x^{max} and ζ_y^{max}, at the probes $(x_0L,0)$ and $(0,x_0L)$ $(x_0=0.4)$ are compared with our asymptotic modal prediction in figures 9–11. We computed these maximum wave elevations as described in appendix B. Readers can see that we accounted for actual positions of the measurement probes as well as contributions given by all nonlinearly involved generalised coordinates, from $O(\eta^{1/3})$ to $O(\eta)$. The authors

https://doi.org/10.1017/jfm.2017.263 Published online by Cambridge University Press

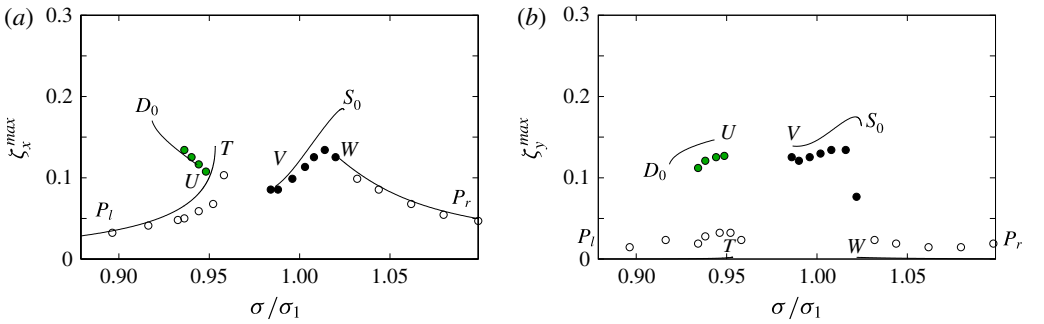


FIGURE 9. The experimental (Ikeda *et al.* 2012) and theoretical L-scaled maximum wave elevations at $(0.4L, 0)$ (marked by ζ_x^{max}) and $(0, 0.4L)$ (ζ_y^{max}) for the longitudinal forcing along the Ox axis. The non-dimensional forcing amplitude is $\eta = \eta_{1a} = 0.00727$ ($\eta_{2a} = 0$) and the mean liquid depth is $h/L = 0.6$. The solid lines denote the computed maximum wave elevations for the stable steady-state regimes. The computations used $\xi = 0.0256$, which corresponds to the experimental logarithmic decrement estimated by Ikeda *et al.* (2012). The empty circles correspond to the experimental planar regime but the filled circles indicate swirling. The grey filled circles correspond in our classification to an almost standing wave in which one from two modified Stokes mode dominates (formally, it is a swirling mode). The theoretical subbranches adopted notations of the response curves in figure 4(*b*).

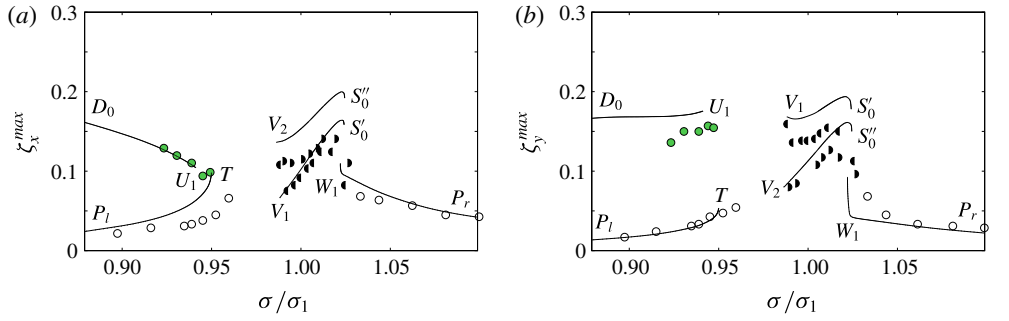


FIGURE 10. The same as in figure 9 but for $\gamma = \pi/6$. The half-circles denote the experimental swirling of the two different angular propagation directions that should theoretically belong, depending on the angular direction, to different branches, either V_1S_0' or V_2S_0''. The response curves in terms of the lowest-order amplitude components A (Ox direction) and B (Oy for this experimental are presented in figure 6*b*).

experience says that working with asymptotic nonlinear solutions of the resonant sloshing problems requires accounting for the higher-order contributions. Finally, we do not speculate with the damping coefficients but use $\xi = 0.0256$, which Ikeda *et al.* (2012) experimentally found by estimating the logarithmic decrements.

The theoretical stable steady-state wave elevations are marked in figures 9–11 by the solid lines. The experimental notation symbols are partly adopted from the corresponding figures by Ikeda *et al.* (2012). Empty circles mark the measured maximum wave elevations for standing waves (planar and diagonal), the green/grey filled circles appear in figures 9 and 10 to specify the almost standing waves. The half-circles (filled) are used to detect the two swirling modes of the different angular

https://doi.org/10.1017/jfm.2017.263 Published online by Cambridge University Press

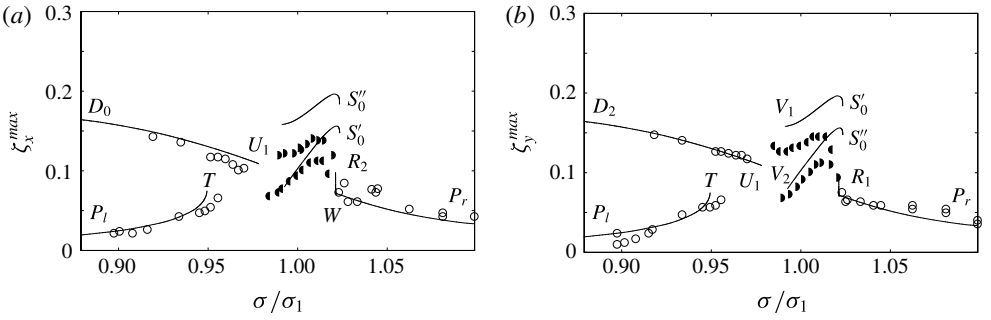


FIGURE 11. The same as in figure 10 but for $\gamma = \pi/4$ (the diagonal forcing). Only diagonal standing waves and swirling are possible. The experimental diagonal waves are marked by empty circles. The half-circles denote the two different experimental swirling modes of the different angular direction. The swirling modes are associated with the subbranches V_1S_0' and V_2S_0'' in figure 8.

directions when these directions dictate non-equal maximum wave elevations at the perpendicular walls. The filled circles are used in figure 9 for the longitudinal forcing where the swirling direction was not important according to Ikeda *et al.* (2012) and our theoretical predictions.

Figure 9 presents the experimental and theoretical results for the longitudinal forcing along the Ox-axis. The theoretical subbranches adopt notations from figure 4. First, we note that the theoretical frequency ranges for the stable steady-state sloshing are generally well predicted, especially for the frequency zone between T (lower bound) and V (upper bound) where irregular waves are theoretically expected. This range was supported by the model tests. However, the theoretical points D_0 and S_0 are located rather far from the experimentally detected ones. Ikeda *et al.* (2012) increased ξ to 0.03 for a more precise theoretical prediction of these points. Our speculative numerical experiments showed this increase really helps for a better fit of these point positions. It also provides a better agreement for ζ_y^{max} in the swirling case. One interesting point is the clearly non-zero experimental values of ζ_y^{max} for the planar-wave regime (P_lT and WP_r). Accounting for the second- and third-order generalised coordinates makes this elevation non-zero but the actual experimental values are clearly larger. We do not know how to explain this fact.

Figure 10 illustrates the theoretical and experimental maximum steady-state wave elevations for the oblique forcing with $\gamma = \pi/6$. The response curves in terms of the lowest-order amplitude components A (Ox direction) and B (Oy) for this experimental case are presented in figure 6(b). The half-circles denote the experimental swirling modes of the two different angular directions that should theoretically belong to either V_1S_0' or V_2S_0'' of figure 6(b). Again, we should remark on a problem in a precise prediction of the larger swirling amplitude of the two swirling modes for both ζ_x^{max} and ζ_y^{max}, which can be fixed by a speculatively increase of the damping coefficient ξ from 0.0256 to 0.03. Because this happens for the larger wave elevations, this may be related to the dynamic contact angle damping, as Keulegan (1959) suggested. This kind of damping (Shukhmurzaev 1997) is of the nonlinear nature and, therefore, may increase with amplitude.

Figure 11 focuses on the diagonal forcing with $\gamma = \pi/4$. A difference from figures 9 and 10 is the absence of the grey circles marking the almost standing wave regime. We expect only stable diagonal and swirling waves. The first one is well predicted,

https://doi.org/10.1017/jfm.2017.263 Published online by Cambridge University Press

but, as was mentioned earlier, the asymptotic theory cannot well approximate the maximum wave elevation for the swirling modes.

One must note that Ikeda *et al.* (2012) performed their own computations. An adaptive multimodal theory was used. Their theoretical results may look better than our computations in some frequency ranges where swirling occurs but have a similar precision for other frequency ranges. We did not compare our asymptotic modal steady-state results with their computations. The reasons for that are that, first, Ikeda *et al.* (2012) neglected the $O(\eta^{2/3})$ and $O(\eta)$ generalised coordinates when computing the elevations, which must, in our opinion, be included, secondly, they adopted a speculatively larger $\xi = 0.03$ for a better fit to the experimental measurements, thirdly, the authors most probably (we did not find an answer in the text) did not account for the actual positions of the measurement probes. As we remarked above, after adopting the speculatively larger ξ, our results would possess a better accuracy for swirling.

8. Conclusions

A motivation for starting this study has been a series of qualitative differences between theoretical and experimental results, which we and some other authors obtained for the resonant sloshing in a square-base tank, and experiments and computations by Ikeda *et al.* (2012). These were discussed in the introduction and denoted as differences between (i)–(iii) and (i′)–(iii′). After realising that these differences can be clarified by the linear damping effect, which may be rather important for relatively small laboratory tanks, we found a lack of knowledge on the undamped resonant sloshing (expected for large containers) when the forcing is neither longitudinal nor diagonal. This caused the threefold goal of the present paper. First, we generalise Part 1 for the oblique forcing. Second, we estimate when the linear damping can be important, establishing, in particular, that it really can matter for the laboratory tests by Ikeda *et al.* (2012) but can be neglected for our earlier experiments. Third, we mathematically explain the aforementioned differences as well as performed some computations to compare the response curves for the damped and undamped cases. All the results remain true for the liquid depth-to-tank width ratio $0.5 \lesssim h/L$ as we have discussed in the context of figure 3.

For the undamped resonant steady-state sloshing, we were able to find an analytical solution of the corresponding secular (necessary solvability condition) system for any oblique forcing. Based on this solution, one concludes that there are theoretically possible, for a given forcing frequency, a maximum of six different standing steady-state resonant waves. Each point on the corresponding response curves determines a single steady-state wave from these six solutions. On the contrary, Part 1 reports maximum three standing waves for longitudinal and diagonal harmonic excitations, which consist of one planar and two square-likes resonant waves so that any point on the square-like response curves corresponds to the two physically identical Stokes waves occurring with an angle to the excitation plane. Each point on the undamped swirling response curves corresponds to physically identical swirling waves (clockwise and counterclockwise).

The main results on the damped resonant sloshing are: (i) the standing resonant waves exist only for longitudinal and diagonal harmonic excitations, these are of planar or diagonal types, respectively, (ii) the square-like standing waves are impossible, (iii) for the oblique non-diagonal forcing with $0 < \delta < 1$, all the damped steady-state sloshing regimes are of the swirling type, (iv) under the asymptotic

https://doi.org/10.1017/jfm.2017.263 Published online by Cambridge University Press

condition (5.15), the damped swirling may become close to a standing wave by a modified Stokes mode so that the resonant sloshing can be treated as an almost standing wave, (v) two physically identical swirling waves of the opposite angular direction are only possible for the longitudinal forcing, (vi) for the oblique forcing, each point on the response curves implies a swirling wave whose amplitudes along the Ox and Oy axes are never equal, even for diagonal forcing. These results make it possible to explain the differences between (i)–(iii) and (i′)–(iii′) described in the introduction. The results are extensively discussed by using the numerical response curves. The damped sloshing response curves are also compared with those for the undamped ones. The latter comparison showed that a complex effect of the non-zero damping and angle γ between the forcing direction and the Ox-axis may significantly change both the branchings and the effective frequency ranges for swirling. Introducing the linear viscous damping is relevant for small-size laboratory tanks and very special applications exemplified by the packaging machines for the tetra-pack cardboard cartons.

We compared our results with the measured maximum wave elevations by Ikeda *et al.* (2012). A satisfactory agreement was found. The agreement for swirling can be improved by a speculative increase of the damping coefficient as Ikeda *et al.* (2012) has done. Because the maximum discrepancy happens for the larger swirling elevations, this increase can be qualitatively argued by nonlinear dynamic contact angle damping (Shukhmurzaev 1997) and strongly nonlinear free-surface phenomena. In this context, the asymptotic linear damping ratio (3.3) makes it possible to evaluate only a lower bound for the total energy dissipation per cycle. However, to the authors' best knowledge, the literature does not give a method for quantifying the dynamic contact angle effect on the logarithmic decrements.

Acknowledgement

The authors acknowledge the financial support of the Centre of Autonomous Marine Operations and Systems (AMOS) whose main sponsor is the Norwegian Research Council (project number 223254–AMOS).

Supplementary materials

Supplementary materials are available at https://doi.org/10.1017/jfm.2017.263.

Appendix A. The steady-state asymptotic solution of (2.6)–(2.7)

Following Faltinsen *et al.* (2003) and using (2.9), (3.2), we can derive an analytical solution of (2.6)–(2.7) in terms of $\epsilon^{1/3}$. The analytical procedure starts with the lowest-order approximation (4.1), which, being substituted into (2.6*c*)–(2.6*e*) gives

$$a_2 = p_0(a^2+\bar{a}^2) + h_0(a^2-\bar{a}^2)\cos 2\bar{\sigma}t + 2h_0 a\bar{a}\sin 2\bar{\sigma}t + O(\epsilon), \quad (\mathrm{A}\,1a)$$

$$b_2 = p_0(\bar{b}^2+b^2) + h_0(\bar{b}^2-b^2)\cos 2\bar{\sigma}t + 2h_0\bar{b}b\sin 2\bar{\sigma}t + O(\epsilon), \quad (\mathrm{A}\,1b)$$

$$c_1 = p_1(a\bar{b}+\bar{a}b) + h_1(a\bar{b}-\bar{a}b)\cos 2\bar{\sigma}t + h_1(\bar{a}\bar{b}+ab)\sin 2\bar{\sigma}t + O(\epsilon), \quad (\mathrm{A}\,1c)$$

where

$$p_0 = \frac{d_4-d_5}{2\bar{\sigma}_{2,0}^2}; \quad h_0 = \frac{d_4+d_5}{2(\bar{\sigma}_{2,0}^2-4)}; \quad p_1 = \frac{\hat{d}_1+\hat{d}_2-\hat{d}_3}{2\bar{\sigma}_{1,1}^2}; \quad h_1 = \frac{\hat{d}_1+\hat{d}_2+\hat{d}_3}{2(\bar{\sigma}_{1,1}^2-4)}. \quad (\mathrm{A}\,2a\text{–}d)$$

Owing to (2.9*e*) (no secondary resonance condition), coefficients p_0, h_0, p_1 and h_1 are formally of $O(1)$.

https://doi.org/10.1017/jfm.2017.263 Published online by Cambridge University Press

Furthermore, inserting (4.1) and (A 1) into (2.6*a*) and (2.6*b*) and gathering the first Fourier harmonic we derive the solvability (secularity) equations (4.3) with respect to the unknown amplitude parameters $a, \bar{a}, b$ and $\bar{b}$. After finding $a, \bar{a}, b$ and $\bar{b}$ from (4.3) and gathering the superharmonics in (2.6*a*) and (2.6*b*), we get

$$\begin{aligned} a_1 \;=\; & a\cos\bar{\sigma}t + \bar{a}\sin\bar{\sigma}t + \big\{[a(n_1(-a^2+3\bar{a}^2)+n_2(b^2-\bar{b}^2))+2n_2b\bar{a}\bar{b}]\cos 3\bar{\sigma}t \\ & + [\bar{a}(n_1(\bar{a}^2-3a^2)+n_2(b^2-\bar{b}^2))-2n_2ab\bar{b}]\sin 3\bar{\sigma}t\big\}/(9-\bar{\sigma}_{1,0}^2)+O(\epsilon), \end{aligned} \tag{A 3}$$

$$\begin{aligned} b_1 \;=\; & \bar{b}\cos\bar{\sigma}t + b\sin\bar{\sigma}t + \big\{[\bar{b}(n_1(-\bar{b}^2+3b^2)+n_2(\bar{a}^2-a^2))+2n_2ab\bar{a}]\cos 3\bar{\sigma}t \\ & + [b(n_1(b^2-3\bar{b}^2)+n_2(\bar{a}^2-a^2))-2n_2a\bar{a}\bar{b}]\sin 3\bar{\sigma}t\big\}/(9-\bar{\sigma}_{0,1}^2)+O(\epsilon), \end{aligned} \tag{A 4}$$

where $n_1 = d_2/2 + h_0((3/2)d_1 + 2d_3)$, $n_2 = (d_6 + d_8 + d_{10} + d_{11})/4 + h_1(d_7/2 + 2d_9 + d_{12})$, $N_1 = -(3/4)q_2 + q_4/4 + h_0(-q_1/2 - 2q_3 + q_5) - q_1p_0$, and $N_2 = q_2/4 + q_4/4 + h_0(q_1/2 + 2q_3 + q_5)$.

In a similar way, one can get

$$\begin{aligned} a_3 \;=\; & \{N_1(a^2+\bar{a}^2)[a\cos\bar{\sigma}t + \bar{a}\sin\bar{\sigma}t] - P_{3,0}\eta_{1a}\cos\bar{\sigma}t\}/(1-\bar{\sigma}_{3,0}^2) \\ & + N_2\{a(-a^2+3\bar{a}^2)\cos 3\sigma t + \bar{a}(\bar{a}^2-3a^2)\sin 3\sigma t\}/(9-\bar{\sigma}_{3,0}^2)+O(\epsilon), \end{aligned} \tag{A 5}$$

$$\begin{aligned} c_{21} \;=\; & \{(N_3\bar{a}^2\bar{b} + (N_4-N_3)ab\bar{a} + N_4a^2\bar{b})\cos\bar{\sigma}t + (N_3a^2b + (N_4-N_3)a\bar{b}\bar{a} \\ & + N_4\bar{a}^2b)\sin\bar{\sigma}t\}/(1-\bar{\sigma}_{2,1}^2) + N_5\{(\bar{a}^2\bar{b} + 2ab\bar{a} - a^2\bar{b})\cos 3\bar{\sigma}t \\ & + (b\bar{a}^2 - 2a\bar{a}\bar{b} - a^2b)\sin 3\bar{\sigma}t\}/(9-\bar{\sigma}_{2,1}^2) + O(\epsilon), \end{aligned} \tag{A 6}$$

$$\begin{aligned} c_{12} \;=\; & \{(N_3ab^2 + (N_4-N_3)b\bar{a}\bar{b} + N_4a\bar{b}^2)\cos\bar{\sigma}t + (N_3\bar{b}^2\bar{a} + (N_4-N_3)b\bar{b}a \\ & + N_4b^2\bar{a})\sin\bar{\sigma}t\}/(1-\bar{\sigma}_{1,2}^2) + N_5\{(ab^2 + 2\bar{a}b\bar{b} - a\bar{b}^2)\cos 3\bar{\sigma}t \\ & + (\bar{a}b^2 - 2ab\bar{b} - \bar{a}\bar{b}^2)\sin 3\bar{\sigma}t\}/(9-\bar{\sigma}_{1,2}^2) + O(\epsilon), \end{aligned} \tag{A 7}$$

$$\begin{aligned} b_3 \;=\; & \{N_1(\bar{b}^2+b^2)[\bar{b}\cos\bar{\sigma}t + b\sin\bar{\sigma}t] - P_{0,3}\eta_{2a}\cos\bar{\sigma}t\}/(1-\bar{\sigma}_{0,3}^2) \\ & + N_2\{\bar{b}(-\bar{b}^2+3b^2)\cos 3\bar{\sigma}t + b(b^2-3\bar{b}^2)\sin 3\bar{\sigma}t\}/(9-\bar{\sigma}_{0,3}^2)+O(\epsilon) \end{aligned} \tag{A 8}$$

from (2.7). Here, $N_3 = -q_7/4 - q_9/4 + (3/4)q_{12} - q_{13}/4 + h_0(q_8/2 + 2q_{10} - q_{15}) - q_8p_0 + h_1(-q_6/2 - 2q_{11} + q_{14})$, $N_4 = -(3/4)q_7 - (3/4)q_9 + q_{12}/4 + q_{13}/4 + h_0(-q_8/2 - 2q_{10} + q_{15}) - q_8p_0 + h_1(-q_6/2 - 2q_{11} + q_{14}) - q_6p_1$, $N_5 = q_7/4 + q_9/4 + q_{12}/4 + q_{13}/4 + h_0(q_8/2 + 2q_{10} + q_{15}) + h_1(q_6/2 + 2q_{11} + q_{14})$.

Appendix B. Theoretical steady-state wave elevations at the walls

Experiments by Faltinsen *et al.* (2003) and Ikeda *et al.* (2012) deal with measurements of the maximum steady-state wave elevations at the perpendicular walls. The measurements were done slightly away from the walls. For brevity, we can associate the positions of the measured probes with the coordinates $\zeta_x : (Lx_0/2,\ 0)$ and $\zeta_y : (0,\ Ly_0/2)$.

Neglecting the linearly involved generalised coordinates and using the notations

$$\left.\begin{aligned} -x_1 = f_1^{(1)}(x_0), \quad -y_1 = f_1^{(2)}(y_0), \quad x_2 = f_2^{(1)}(x_0), \quad y_2 = f_2^{(2)}(x_0), \\ -x_3 = f_3^{(1)}(x_0), \quad -y_3 = f_3^{(2)}(y_0) \end{aligned}\right\} \tag{B 1}$$

https://doi.org/10.1017/jfm.2017.263 Published online by Cambridge University Press

computes the wave elevations at ζ_x and ζ_y as

$$\zeta_x(t) = -x_1 a_1(t) + x_2 a_2(t) - b_2(t) - x_3 a_3(t) + x_1 c_{12}(t), \tag{B 2a}$$
$$\zeta_y(t) = -y_1 b_1(t) - a_2(t) + y_2 b_2(t) - y_3 b_3(t) + y_1 c_{21}(t), \tag{B 2b}$$

where the nonlinearly governed generalised coordinates are accounted for. Substituting the steady-state solution from appendix A into (B 2) derives the following expressions to approximate the steady-state wave elevations:

$$\begin{aligned}
\zeta_x(t) \;=\; & p_0[x_2(a^2+\bar a^2) - (b^2+\bar b^2)] \\
& + \boxed{\cos\bar\sigma t}\,[-x_1 a - x_3(N_1 a(a^2+\bar a^2) - P_{3,0}\eta_{1a})/(1-\bar\sigma_{3,0}^2) \\
& + x_1(N_3 a b^2 + (N_4 - N_3) b\bar a\bar b + N_4 a\bar b^2)/(1-\bar\sigma_{1,2}^2)] \\
& + \boxed{\sin\bar\sigma t}\,[-x_1\bar a - x_3 N_1\bar a(a^2+\bar a^2)/(1-\bar\sigma_{3,0}^2) \\
& + x_1(N_3\bar b^2\bar a + (N_4 - N_3) b\bar b a + N_4 b^2\bar a)/(1-\bar\sigma_{1,2}^2)] \\
& + \boxed{\cos 2\bar\sigma t}\,[h_0(x_2(a^2-\bar a^2) - (\bar b^2 - b^2))] + \boxed{\sin 2\bar\sigma t}\,[2h_0(x_2 a\bar a - \bar b b)] \\
& + \boxed{\cos 3\bar\sigma t}\,[-x_1(a[n_1(-a^2+3\bar a^2) + n_2(b^2-\bar b^2)] + 2n_2 b\bar a\bar b)/(9-\bar\sigma_{1,0}^2) \\
& - x_3 N_2 a(-a^2+3\bar a^2)/(9-\bar\sigma_{3,0}^2) + x_1 N_5(ab^2 + 2\bar a b\bar b - a\bar b^2)/(9-\bar\sigma_{1,2}^2)] \\
& + \boxed{\sin 3\bar\sigma t}\,[-x_1(\bar a[n_1(\bar a^2 - 3a^2) + n_2(b^2-\bar b^2)] - 2n_2 ab\bar b)/(9-\bar\sigma_{1,0}^2) \\
& - x_3 N_2\bar a(\bar a^2 - 3a^2)/(9-\bar\sigma_{3,0}^2) + x_1 N_5(\bar a b^2 - 2ab\bar b - \bar a\bar b^2)/(9-\bar\sigma_{1,2}^2)]; \quad \text{(B 3a)}
\end{aligned}$$

$$\begin{aligned}
\zeta_y(t) \;=\; & p_0[-(a^2+\bar a^2) + y_2(b^2+\bar b^2)] \\
& + \boxed{\cos\bar\sigma t}\,[-y_1\bar b - y_3(N_1\bar b(\bar b^2+b^2) - P_{0,3}\eta_{2a})/(1-\bar\sigma_{0,3}^2) \\
& + y_1(N_3\bar a^2\bar b + (N_4 - N_3) ab\bar a + N_4 a^2\bar b)/(1-\bar\sigma_{2,1}^2)] \\
& + \boxed{\sin\bar\sigma t}\,[-y_1 b - y_3 N_1 b(b^2+\bar b^2)/(1-\bar\sigma_{3,0}^2) \\
& + y_1(N_3 a^2 b + (N_4 - N_3) a\bar a\bar b + N_4\bar a^2 b)/(1-\bar\sigma_{2,1}^2)] \\
& + \boxed{\cos 2\bar\sigma t}\,[h_0(-(a^2-\bar a^2) + y_2(\bar b^2 - b^2))] + \boxed{\sin 2\bar\sigma t}\,[2h_0(-a\bar a + y_2\bar b b)] \\
& + \boxed{\cos 3\bar\sigma t}\,[-y_1(\bar b[n_1(-\bar b^2+3b^2) + n_2(\bar a^2 - a^2)] + 2n_2 ab\bar a)/(9-\bar\sigma_{0,1}^2) \\
& - y_3 N_2\bar b(-\bar b^2+3b^2)/(9-\bar\sigma_{0,3}^2) + y_1 N_5(\bar a^2\bar b + 2ab\bar a - a^2\bar b)/(9-\bar\sigma_{2,1}^2)] \\
& + \boxed{\sin 3\bar\sigma t}\,[-y_1(b[n_1(b^2 - 3\bar b^2) + n_2(\bar a^2 - a^2)] - 2n_2 a\bar a\bar b)/(9-\bar\sigma_{0,1}^2) \\
& - y_3 N_2 b(b^2 - 3\bar b^2)/(9-\bar\sigma_{0,3}^2) + y_1 N_5(b\bar a^2 - 2a\bar a\bar b - a^2 b)/(9-\bar\sigma_{2,1}^2)]\,. \quad \text{(B 3b)}
\end{aligned}$$

The maximum theoretical wave elevations at the two measured probes are, therefore, associated with the maximum of the truncated series on the interval $[0, 2\pi]$.

REFERENCES

DUCCI, A. & WEHELIYE, W. H. 2014 Orbitally shaken bioreactors-viscosity effects on flow characteristics. *AIChE J.* **60** (11), 3951–3968.

FALTINSEN, O. M., ROGNEBAKKE, O. F. & TIMOKHA, A. N. 2003 Resonant three-dimensional nonlinear sloshing in a square-base basin. *J. Fluid Mech.* **487**, 1–42.

https://doi.org/10.1017/jfm.2017.263 Published online by Cambridge University Press

FALTINSEN, O. M., ROGNEBAKKE, O. F. & TIMOKHA, A. N. 2005*a* Classification of three-dimensional nonlinear sloshing in a square-base tank with finite depth. *J. Fluids Struct.* **20** (1), 81–103.

FALTINSEN, O. M., ROGNEBAKKE, O. F. & TIMOKHA, A. N. 2005*b* Resonant three-dimensional nonlinear sloshing in a square-base basin. Part 2. Effect of higher modes. *J. Fluid Mech.* **523**, 199–218.

FALTINSEN, O. M., ROGNEBAKKE, O. F. & TIMOKHA, A. N. 2006*a* Resonant three-dimensional nonlinear sloshing in a square-base basin. Part 3. Base ratio perturbation. *J. Fluid Mech.* **551**, 93–116.

FALTINSEN, O. M., ROGNEBAKKE, O. F. & TIMOKHA, A. N. 2006*b* Transient and steady-state amplitudes of resonant three-dimensional sloshing in a square base tank with a finite fluid depth. *Phys. Fluids* **18**, 012103.

FALTINSEN, O. M. & TIMOKHA, A. N. 2009 *Sloshing*. Cambridge University Press.

GRUNDELIUS, M. 2001 Methods for control of liquid slosh. PhD thesis, Department of Automatic Control, Lund Institute of Technology, Sweden.

HENDERSON, D. M. & MILES, J. W. 1994 Surface-wave damping in a circular cylinder with a fixed contact line. *J. Fluid Mech.* **275**, 285–299.

IKEDA, T., HARATA, Y. & OSASA, T. 2016 Internal resonance of nonlinear sloshing in rectangular liquid tanks subjected to obliquely horizontal excitation. *J. Sound Vib.* **361**, 210–225.

IKEDA, T., IBRAHIM, R. A., HARATA, Y. & KURIYAMA, T. 2012 Nonlinear liquid sloshing in a square tank subjected to obliquely horizontal excitation. *J. Fluid Mech.* **700**, 304–328.

KEULEGAN, G. 1959 Energy dissipation in standing waves in rectangular basins. *J. Fluid Mech.* **6** (1), 33–50.

PILIPCHUK, V. N. 2013 Nonlinear interactions and energy exchange between liquid sloshing modes. *Physica* D **263**, 21–40.

ROYON-LEBEAUD, A., HOPFINGER, E. J. & CARTELLIER, A. 2007 Liquid sloshing and wave breaking in circular and square-base cylindrical containers. *J. Fluid Mech.* **577**, 467–494.

SHUKHMURZAEV, YU. D. 1997 Moving contact lines in liquid/liquid/solid systems. *J. Fluid Mech.* **334**, 211–249.

WU, C.-H. & CHEN, B.-F. 2009 Sloshing waves and resonance modes of fluid in a 3D tank by a time-independent finite difference method. *Ocean Engng* **36**, 500–510.

WU, C.-H., CHEN, B.-F. & HUNG, T.-K. 2013*a* Hydrodynamic forces induced by transient sloshing in a 3D rectangular tank due to oblique horizontal excitation. *Comput. Math. Appl.* **65**, 1163–1186.

WU, C.-H., FALTINSEN, O. M. & CHEN, B.-F. 2013*b* Analysis on shift of nature modes of liquid sloshing in a 3D tank subjected to oblique horizontal ground motions with damping devices. *Adv. Mech. Engng* 627124.

ZHANG, H.-S., WU, P.-F. & LIU, W.-B. 2014 The analysis of second-order sloshing resonance in a 3-D tank. *J. Hydrodyn.* **26** (2), 309–315.

https://doi.org/10.1017/jfm.2017.263 Published online by Cambridge University Press